How do the products in methane dehydroaromatization impact the distinct stages of the reaction?

Antoine Beuque, Hu Hao, Elise Berrier, Nuno Batalha, Alexander Sachse, Jean-François Paul, Ludovic Pinard

How the products in methane dehydroaromatization impact each different stage of the reaction?

Antoine Beuque[1], Hu Hao[2], Elise Berrier [2], Nuno Batalha [1], Alexander Sachse [1], Jean-François Paul* [2], Ludovic Pinard [1,*]

[1]Institut de Chimie des Milieux et Matériaux de Poitiers (ICM2P), UMR 7285 CNRS, 4 Rue Michel Brunet, Bâtiment B27, 86073 Poitiers Cedex 9–France;

[2]Univ. Lille, CNRS, Centrale Lille, Univ. Artois, UMR 8181–UCCS–Unité de Catalyse et Chimie du Solide, F-59000 Lille, France).

*Corresponding authors: jean-francois.paul@univ-lille.fr, ludovic.pinard@univ-poitiers.fr

Abstract

Methane dehydroaromatization reaction at 700 °C over Mo/ZSM-5 involves numerous changes of the molybdenum species from the catalyst preparation and throughout the catalyst lifetime, composed of 4 successive steps: calcination, activation, induction, and deactivation.

In the frame of investigating the transformation phenomena undertaken by the catalyst during each stage of the reaction, the methane gas hourly space velocity per gram of catalyst (M-GHSV) was subsequently changed from 1 to 29 $L_{CH4}\,h^{-1}\,g_{cat}^{-1}$. From this kinetic study, unexpected behaviors start to emerge. Modeling was then carried out to support those initial results.

It appears, MoO_3 firstly reacts stoichiometrically during the calcination (ΔrH =0.86 eV) with bridged hydroxyl pairs yielding $[Mo_2O_5]^{2+}$ (calcination). After which, $Mo_2O_5^{2+}$ is slowly reduced by methane to form $Mo_2C_2^{2+}$ (activation). The latter converts methane to ethylene (E_A= 1.49 eV), which dimerizes two times faster to butene through a hydrocarbon pool than on Brønsted acid sites (induction). The catalyst deactivates through an inhibition effect of aromatics, which adsorbs strongly onto $Mo_2C_2^{2+}$ (ΔH_{ads} ~ 0.7 eV) (deactivation). Yet, the large amount of autogenous hydrogen produced at lower space velocity allows preventing the active species poisoning, which achieves a slower deactivation rate.

Keywords: Zeolite, methane dehydroaromatization, deactivation molybdenum, carbides, hydrogen

1. Introduction

As world reserves of readily accessible petroleum are progressively being depleted, natural gas strongly emerged as an abundant, versatile, and profitable alternative feedstock allowing for lower carbon emissions due to its high H/C ratio. Methane, the main natural gas component, is primarily used as electricity supply. As only 1.5% of natural gas is catalytically converted into high-added value chemicals, groundbreaking methods for the transformation of methane are considerably required. [1 2]

Methane dehydroaromatization (MDA: 6 $CH_4 \leftrightharpoons C_6H_6 + 9\ H_2$) under non-oxidative conditions over Mo/HZSM-5 has received significant interest over the past three decades. [3] This direct route allows to highly selectivly decarbonizing methane into benzene (~ 70 wt. %) while simultaneously producing sustainable hydrogen, which offers great potential as future energy resource. Yet, MDA suffers from two key hurdles:

(i) low activity, the one-pass conversion into benzene is thermodynamically limited, i.e., 12.5% at 700 °C.[4 5]

(ii) rapid catalyst deactivation by coking, coke formation catalyzed by Brønsted acid sites is kinetically favored at high temperature.[6 7]

Even if the reaction mechanism and determination of the nature of the exact molybdenum active species are still a matter of discussion, new insights could be gained through operando techniques. It was established that the MDA process occurs through three successive steps [8 9], or rather four when the preparation stage (step 0) is included in the overall process. The latter generally consists of the wet impregnation of a molybdenum salt followed by calcination to stabilize an oxomolybdate phase dispersed on the protonic zeolite to yield Mo/ZSM-5 in fully oxidized form.[10] It is well known that the molybdenum starts to migrate inside the zeolite channels during the calcination step. Once the maximum capacity of exchange is reached, the molybdenum is deposited on the external surface.[11] Both

operating calcination conditions (i.e. temperature [10]) and textural properties of the fresh catalyst (i.e. Mo loading [11], Si/Al ratio [12 13],…) play a key role on the stabilized oxomolybate phases. Molybdenum trioxide MoO_3 on the external surface, MoO_2^{2+} monomers and $Mo_2O_5^{2+}$ dimers bridged with two aluminium pair, $MoO_2(OH)^+$ monomers bridged only with one isolated aluminium or silanol were reported.[14]

Once the as-prepared oxide is synthetized, it needs to be reduced during the so-called activation period (step 1) for which amount of CO_2, H_2, H_2O and CO appears before aromatic production. [15 16 17] The principal purpose of this step is the reduction of the oxomolybdate moieties into Mo (oxy)-carbide identified as the active species of the reaction. A large variety of molybdenum reduced centers such as MoC, α-Mo_2C_{1-x}, β-Mo_2C, MoO_xC_y, partially reduced MoO_{3-x} were reported [18 19] as the active species pointing out the genuine complexity of correctly determining their exact nature.

At the end of this first stage, benzene formation initiates. Its yield increases during the induction period (step 2) and reaches a maximum due to thermodynamic limitations. Catalyst evolution is much more complicated to understand during this short period of time (~ 30min). Recently, new insights were brought to light concerning the possible formation of a hydrocarbon pool (HCP) like mechanism well-known in the methanol to olefin reaction (MTO). [20] Reduced molybdenum species initiate creation of the HCP on BrØnsted acid sites. [9,21] To resume methane is firstly activated on the molybdenum carbide producing light olefins (ethylene, C_2H_x intermediates,…) which interact rapidly with the near Mo-proton acid site to create the HCP responsible for aromatics production. [22]

Once the catalyst achieves its operational activity, it begins to deactivate (step 3). During this deactivation period, carbon deposition on the catalyst is observed. Several studies [23 24] underline three types of formed carbonaceous compounds: i) molybdenum carbide, ii) graphitic carbon deposited as a layer near the molybdenum site (“soft” coke), and iii) polyaromatic compounds on acid sites (“hard” coke). The latter is responsible for catalyst deactivation. [25 26] Kosinov et al.[21] questionned the coke nature distinction and explained polyaromatic compound were deposited inside and outside of the catalyst. The only

observable differences on thermogravimetric analysis were made by the diffusion limitations of the oxygen molecules and the MoO_x-catalyzed combustion of the near surface carbon. Furthermore, recent studies provided new insights into the deactivation trend, emphasizing hydrocarbon pool formation [27] [21] or carbide molybdenum sintering. [28] [29] [30]

In other words, each step brings its share of mystery. To fully understand the complex nature of the involved mechanisms, further insight into the four MDA key steps is required. Indeed, both the involvements of the hydrocarbon pool and the actual molybdenum active sites during steps 1 and 2 still remain under consideration. Likewise, the nature of deactivation in step 3 is widely disputed.

In the following study, methane dehydroaromatization was carried out at 700 °C., and the methane gas hourly space velocity per gram of catalyst (M-GHSV) was subsequently changed from 1 to 29 LCH4 h-1 gcat. Each step of the reaction was deeply investigated thanks to a mass spectroscopy coupled with gas chromatography. It allows us to quantify hydrogen production, which is too often ignored in the MDA. From the quantification of all the products formed during the MDA reaction, it is possible to address the question of their impact on each step of the reaction. This kinetic study paid particular attention to the evolution of structure, localization, and quantification of distinct molybdenum species throughout the defined key steps and their impact on the overall process's activity, selectivity, and stability. Quantification of all formed products confirmed previous statements and raised new insights into this enigmatic reaction.

2. Experimental

Catalyst preparation (step 0). The NH_4-ZSM-5 zeolite from Zeolyst International (CBV 5020) with a molar Si/Al ratio of 25 was calcined under static conditions under air at 550 °C for 6 h with a heating rate of 2 °C min^{-1}. H-ZSM5 (25) was impregnated by traditional incipient wetness impregnation with an 0.0044 M aqueous solution of ammonium heptamolybdate tetrahydrate (AHM, $(NH_4)_6Mo_7O_{24}.4H_2O$), to obtain a Mo loading of 3.1wt.%. The solution was added dropwise in the proportion of 10 mL per gram of zeolite under magnetic stirring

(400 rpm) at 25 °C for 24 h. The catalyst was dried and calcined under static air at 80 °C for 12 h, then at 500 °C for 6h using a heating ramp of 2 °C min^{-1}. The catalyst is denoted Mo/H-ZSM-5.

Characterization of zeolite before and after Mo impregnation. Powder X-ray diffractograms were collected with a PANalytical Empyrean X-ray diffractometer using CuKα radiation (1.54059 Å), for the 2θ range from 5 to 50°. The scan speed was fixed at 0.033° s^{-1}.

The silicon, aluminum, and molybdenum contents of Mo/H-ZSM-5 were determined using Inductively Coupled Plasma-Optical Emission Spectroscopy (ICP-OES) on an Optima 2000 DV (Perkin-Elmer).

Nitrogen sorption measurements were carried out at –196 °C on the zeolite before and after wetness impregnation with a Micromeritics 3Flex apparatus. The fresh samples were outgassed at 450°C and the spents samples at room temperature under vacuum for 15 h before the sorption measurements. The micropore volume (V_{micro}) was calculated from the t-plot curve using the Harkins-Jura method and a thickness range between 4.5 and 5.5 Å.

Raman spectroscopy was carried out using a HORIBA Jobin Yvon LabRAM HR800 confocal Raman microscope with a CCD detector. Spectra were acquired at 25 °C using an excitation wavelength of 532.4 nm. In addition, operando Raman spectroscopy has been applied for monitoring the decomposition of carbon species on spent catalyst during a stepwise temperature increase under 20mL/min of 20% O_2/He mixture at atmospheric pressure. The Raman spectra were collected at desired temperature in confocal mode using the 488 nm line of a Ar^+ laser (5mW at sample, Melles Griot) focused on the sample placed in the flat dome version of the atmospheric chamber (Harrick Scientific) using a 50X long working distance objective (NA: 0.6, Olympus). The scattered light was guided through a 150 µm pinhole, dispersed and collected using a Peltier-cooled CCD implemented within a HORIBA HR equipment. The gaseous products were analyzed in real time using a micro-GC (Agilent).

The nature and concentration of acidity of the zeolite before and after Mo impregnation were studied using pyridine adsorption followed by infrared spectroscopy (FTIR) with a Nicolet 5700 apparatus with 2 cm^{-1} optical resolution. Before analysis, the samples were pressed (0.5 ton) into a self-supporting wafer (2 cm^2) and pre-treated from 20 °C to 450 °C under 100 mL min^{-1} of air stream with a rate of 2°C min^{-1}. The sample was then degassed for 1 h at 200 °C, after which an IR spectrum was taken. The sample was then cooled down to 150 °C, exposed to a pyridine pressure of 1.5 10^{-3} bar for 5 min, and then further degassed for 1 hour before recording the spectra. The concentration of Brønsted (PyH^+) and Lewis acid sites (PyL) (µmol g^{-1}), were calculated using the Beer-Lambert-Bouguer law from the integrated absorbance of the corresponding IR bands (1545 and 1455 cm^{-1}) and the integrated molar adsorption coefficients: ε_{1545} = 1.13 and ε_{1454} = 1.28 cm mol^{-1}. All the reported FTIR spectra are normalized to a wafer density (mg cm^{-2}).

Catalytic test (step 1-2): Methane dehydroaromatization was performed at atmospheric pressure in a fixed-bed quartz reactor (6 mm inner diameter) at 700 °C under continuous feeding with a (15/85) (v/v) N_2/CH_4 mixture (Air Liquid, purity: 99.999%). The flow rate was kept constant at 0.84 L h^{-1} (STP), while the catalyst mass was varied from 0.025 to 0.7 g to change the methane gas hourly space velocity per gram of catalyst (M-GHSV) from 1 to 29 $L_{CH4}\,h^{-1}\,g_{cat}^{-1}$ and contact time (t) from 0.04 to 2.04 s. Before testing, catalysts were compacted under 3 tons, crushed, and sieved to obtain homogeneous particles (0.2-0.4 mm). Samples were pre-treated at 700 °C under nitrogen flow (3 L h^{-1}) for 1 h, using a heating ramp of 10 °C min^{-1}. It is worth mentioning that the experiments performed at the same contact time obtained with different flow rates and catalyst mass gave similar conversion, indicating that no extragranular diffusion limitation occurred.

The gaseous products and hydrogen were analyzed online by a Varian CP-3800 gas chromatograph equipped with an FID detector connected to a fused silica J&W GS-Gaspro capillary column (60 m x 0.32 mm x 4 µm) and a TCD connected to a J&W PoraPLOT Q-HT capillary column (25 m x 0.53 mm x 20 µm). The GC analysis time was 30 min and therefore

does not allow data to be obtained during the activation and induction periods (step 1 and 2); an HPR 20 QIC R&D mass spectrometer (Hiden Analytical) was also connected to the exhaust gas to monitor as a function of time-on-stream the mass-to-charge ratio 16, 27, 78, 92, and 128, which corresponds to CH_4, $C_2H_3^+$, C_6H_6, C_7H_8, and $C_{10}H_8$, respectively.

Spent catalyst characterization (step 3): After 10 h, the feed gas was stopped and switched to a nitrogen flow while the reactor is quenched under an external airflow. The spent catalysts were named Sp/x, where x refers to the contact time. Coke amount was quantified with a SDT Q600 under a flow rate of 100 mL min^{-1} of air up to 900 °C. After loading the TG cell, the sample was firstly kept for 30 min in a dry air stream. The sample was then heated with a rate of 20 °C min^{-1}. Once the final temperature is reached, the plateau was held for 10 min. Burning gas, i.e., H_2O (m/z = 18), CO (m/z = 28), and CO_2 (m/z = 44) were monitored by mass spectra (QGA Hiden Analytical). Residual acidity and microporosity were measured using the same protocol as previously described.

DFT calculations (step 0-3): All DFT calculations were performed using the Vienna Ab Initio Simulation Package (VASP, version 5.4.1). [31] [32] The PBE functional based on the generalized gradient approximation was chosen for the exchange-correlation energy, considering a compromise between accuracy and computational speed.

A Plane-wave basis set combined with the projected augmented wave (PAW) method was used to describe the valence electrons and valence-core interactions. The kinetic energy cut-off of the plane wave basis set was set to 500 eV after having clarified its relevance. Gaussian smearing of the population of partial occupancies with a width of 0.1 eV was used during iterative diagonalization of the Kohn-Sham Hamiltonian. For each iteration, the threshold for energy convergence was set to 10^{-5} eV. The criterion for geometry convergence was assumed to be reached as a force resultant on every atom was lower than 0.05 eV/Å. Brillouin zone sampling was restricted to the G (Gamma) point due to the large size of the used unit cell.

The as-optimized ZSM-5 unit cell is orthogonal with the following lattice parameters: a= 20.241 Å, b= 20.015 Å, and c=13.439 Å using an all-silica MFI structure as starting model. Such unit cell parameters agree with previous DFT studies and experimental data for stabilized ZSM-5 samples.

The adsorption energy of the reaction intermediate was calculated as

$$\Delta E_{ads} = (E_{adsorbate}@Mo/ZSM5) - (E_{adsorbate}) - (E\ Mo/ZSM5) \qquad \text{(eq.1)}$$

thus negative adsorption energy indicates an exothermic adsorption process.

3. Results

3.1. Physico-chemical properties of H-ZSM-5 zeolite before and after molybdenum impregnation

H-ZSM-5 zeolite. Figure 1 compares nitrogen sorption at -196 °C, infrared and Raman spectra and XRD patterns of the H-ZSM-5 zeolite before and after molybdenum impregnation.

The nitrogen adsorption and desorption isotherm (**Figure 1a**) is of type I and displays a strong nitrogen uptake at high relative pressure. This uptake indicates the presence of inter-particular mesopore (0.09 $cm^3\ g^{-1}$) ascribable to crystal aggregation. The microporous volume of 0.14 $cm^3\ g^{-1}$ (**Table 1**) is lower than expected for a conventional well-crystallized MFI-type zeolite, i.e., 0.17 $cm^3\ g^{-1}$. [33] This difference might result from the difficulty in assessing the exact micropore volume by *t*-plot for ZSM-5 zeolites with Si/Al ratios > 20 due to the monoclinic/orthorhombic transition leading to an adsorption step at P/P_0 = 0.2. [34]

Table 1: Textural properties of the protonic and fresh impregnated sample.
(in brackets, the loss or gain after Mo impregnation).

	Mo[a] (wt.%)	[PyH^+][b] (µmol g^{-1})	[PyL][c] (µmol g^{-1})	V_{micro}[d] ($cm^3\ g^{-1}$)	V_{meso}[e] ($cm^3\ g^{-1}$)
H-ZSM-5	0	280	85	0.14	0.09
Mo/H-ZSM-5	3.1	220 (-20%)	124.5 (+46%)	0.12 (-15%)	0.09 (0%)

[a] measured by ICP analysis, [b,c]: concentration of Brønsted and Lewis acid sites probed by thermodesorption of pyridine at 150 °C, [d]Estimated by t-plot method; [e]Mesopore volume= V_{total}-V_{micro} (V_{total}: determined from the adsorbed volume at p/p°= 0.96).

The infrared spectrum in the OH stretching region exhibits four bands (**Figure 1b**). An intense band at 3610 cm^{-1} (± 2) attributed to the bridged hydroxyl groups (Si-O(H)-Al); an asymmetric band at 3740 cm^{-1} ascribable to the terminal silanol groups on the external surface, and two bands at 3665 cm^{-1} and 3785 cm^{-1} (less intense), which correspond to OH linked to extraframework aluminum species (e.g., $AlOH^{+}$). All the bridged hydroxyl groups SiO(H)Al react upon pyridine adsorption at 150 °C, revealing their pure BAS behavior, whereas EFAl (AlOH) and terminal silanols (SiOH) can only partially chemisorb pyridine.

The concentration of the Brønsted acid sites (BAS) able to retain pyridine at this temperature is 280 µmol g^{-1} (**Table 1**), reaching 43% of the total Al content of 640 µmol g^{-1}. This difference means that 30-40 % of the theoretical protons exist as BAS, with the other distributed among the other distorted framework sites or other non-framework sites. [35]

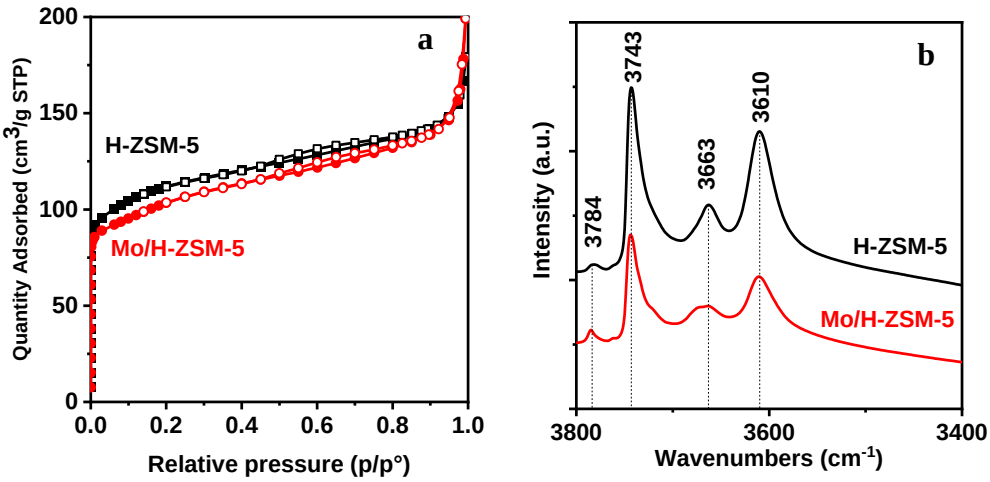

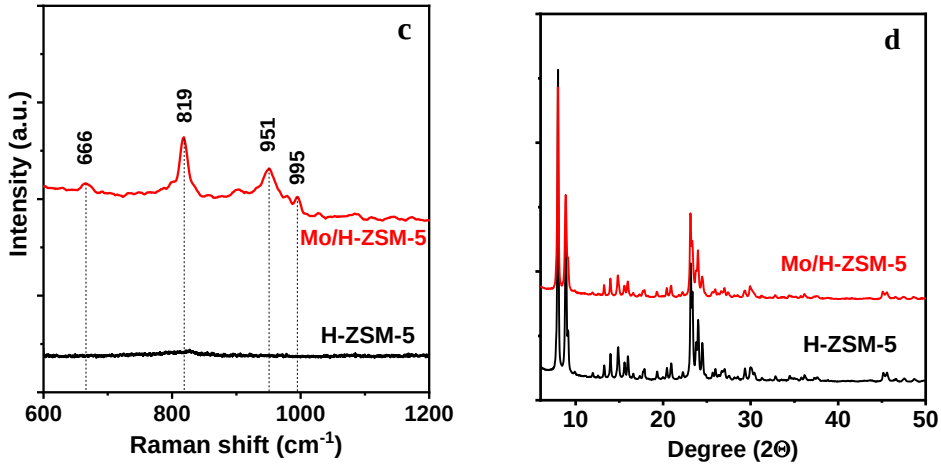

Figure 1: Characterization of the H-ZSM-5 before and after Mo impregnation: (a) N_2 adsorption and desorption isotherms, (b) IR spectra of OH region, (c) Raman spectra and XRD patterns.

Step 0: H-ZSM-5 supported oxomolybdate phases. The impregnation of H-ZSM-5 by an aqueous solution of AHM ($(NH_4)_6Mo_7O_{24}.4H_2O$) followed by static calcination yields Mo/ZSM-5 with a molybdenum content of 3.1 wt.%. Mo enrichment leads to a loss of the micropore volume (-15%, **Table 1**) and a decrease in the intensity of bridged hydroxyl IR band (-20%) in the same proportion of the concentration of Brønsted acid sites) (**Figure 1a and Table 1**). The loss of BAS suggests a reaction between the molybdenum oxide and the protonic site.

During the calcination process, AHM decomposes into neutral volatile molybdenum oxide oligomers. [36] Among the latter, MoO_3 and Mo_2O_6 species can diffuse inside sinusoidal and straight channels of the H-ZSM-5 zeolite[11] to react with BAS sites, mostly consistent with the

bridged hydroxyl groups Si-O(H)-Al. A systematic study detailed by Pidko *et al.* convincingly states that the most stable adsorption structure for molybdenum within the ZSM-5 channels is consistent with a Mo_2O_5 dimer bridging two Al centers within the six-membered rings 6MR-δ located at the intersections between the straight and tortuous channels. [37] We modeled the adsorption energies of a MoO_3 monomer and a Mo_2O_5 dimer on bridging hydroxyl groups showing Al in the next nearest neighbor (NNN) positions (**Scheme 1).**

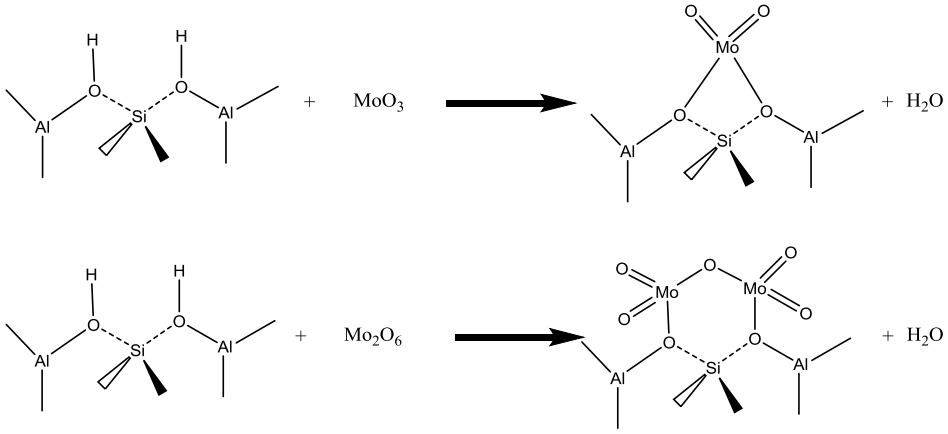

Scheme 1. Anchoring sites of Molyddemun oxide.

The formation of the dimeric species is only slightly endothermic (0.85 eV), while the formation of the monomeric species is more endothermic (3.50 eV). The corresponding structures of both monomeric and dimeric oxomolybdate phases are shown in **Figure S1**. Hence, our calculations are in good agreement with what was proposed by Pidko et al.[37] The most stable adsorption structure for molybdenum within the ZSM-5 channels is the dimer Mo_2O_5 bridged at two Al atoms in 6MR-δ.

Rice et al.[38] calculated by stochastic simulations the probability in ZSM-5 zeolite of NNN pairs of Al atoms able to stabilize a divalent cation (M^{2+}) and form an oxo- binuclear cation, i.e., two M^{2+} bridged by an oxygen atom $(-M-O-M-)^{2+}$. The assessment of the maximum probability to form bridged M^{2+} cations is 0.07 with a Si/Al of 24. Relative to the binuclear oxo metal cation, the possibility is higher: 0.19. This proportion is consistent with the loss of BAS concentration (-20 %, **Table 1**), suggesting that the residual proton sites are isolated. The amount of Mo at the channel intersections is therefore limited to the number of aluminum

pairs. From the residual acidity measurement, speciation of Mo moieties can be established. The amount of Mo involved in dimeric oxomolybdate supported on the zeolite framework is: $(280 - 220) \times 10^{-6} \times M_{Mo} \times 100 = 0.58\, wt.\%$, with M_{Mo} = 95.95 g mol^{-1}. Most remaining $3.1 - 0.58 = 2.52\, wt.\%$ Mo is assumed to be located on the external surface of the zeolite in the form of tri-dimensional MoO_3. The presence of the latter is confirmed by the appearance of high-intensity peaks at 666, 815, and 995 cm^{-1} in the Raman spectrum [39, 40] **(Figure 1c)**. The absence of characteristic peaks in the XRD pattern (**Figure 1d**) of the orthorhombic MoO_3 at 12.7°, 25.7°, and 27.3° [41] indicates the presence of MoO_3 phase with small diffraction domains (below 10 nm).

It is worth mentioning the possible presence of a third molybdenum species located on the outer surface of the zeolite crystals. After the calcination step, the intensity of the external silanol band partially decreases (**Figure 1b**). By analogy with Al pairs, the assumption was established that vicinal silanols could further react with molybdenum oxide (**Scheme 2**):

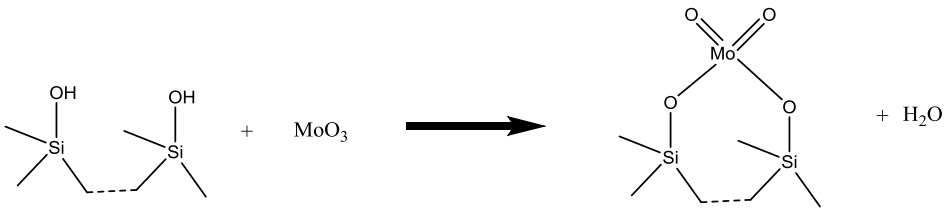

(eq. 4)

Scheme 2. Anchoring sites of molybdenum oxide on external silanols.

The previous characterizations indicate three different types of molybdenum species on the fresh catalyst: (i) anchored molybdenum on BAS (0.6 wt. %), (ii) MoO_3 on the external surface as small dispersed clusters (2.5 wt. %) and (iii) a small portion of anchored molybdenum on the external silanol sites.

3.2. Stages of methane dehydroaromatization reaction

The transformation of methane is carried out at 700 °C under atmospheric pressure. **Figure 2a** displays the mass-to-charge ratio of 78 m/z, which corresponds to benzene, as a function of the time-on-stream. After a product-free period, benzene appears rapidly, followed by a slight decrease. Thus, three successive steps occur during the MDA reaction: activation with

no aromatics production (step 1), induction (step 2), and slow deactivation (step 3). For that reason, three states of the molybdenum species can be considered:

1) oxomolybdate phases before the activation period;
2) carbide species at the beginning of the reaction (0.5 h, catalyst exempt of coke);
3) deactivated carbides after 10 h of reaction.

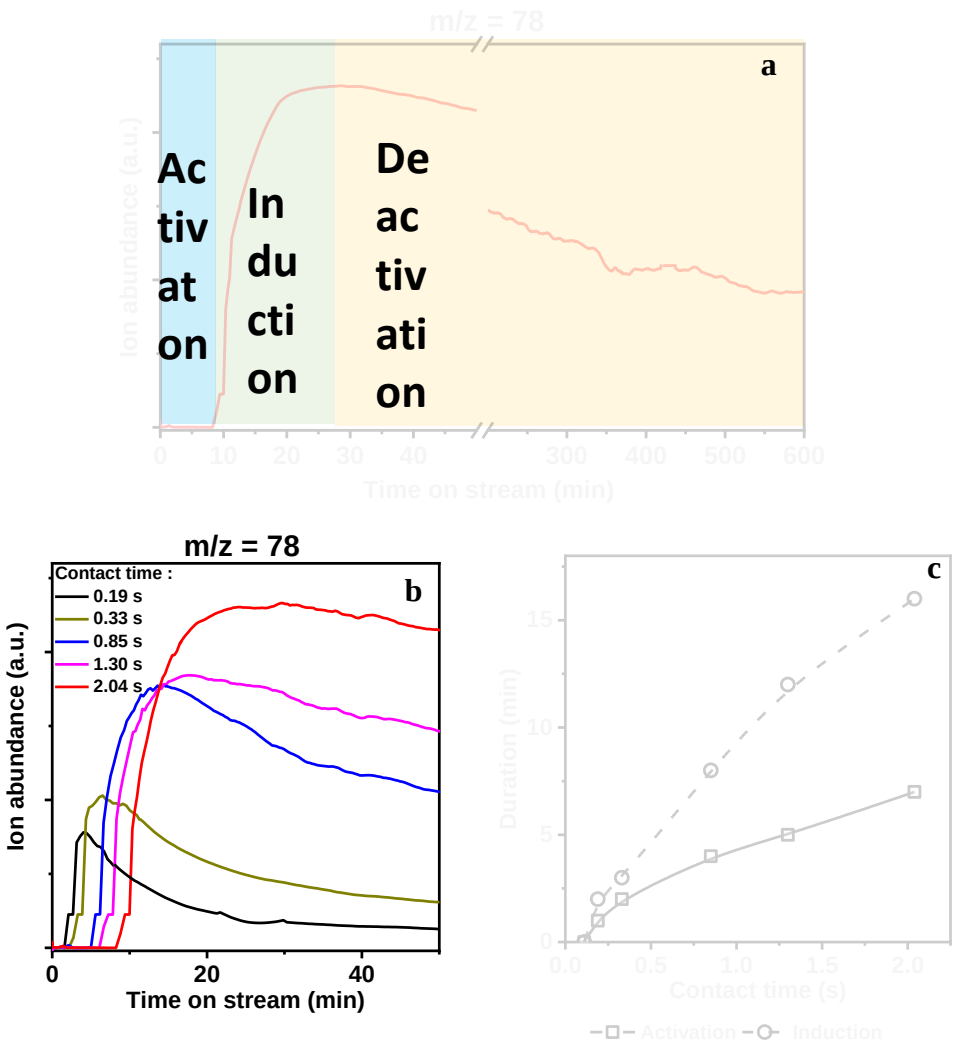

Figure 2: (a) Ion abundance of benzene as a function of a long time-on stream, (b) for different contact times during activation and inductions, and (c) duration of these two steps as a function of contact time.

Step 1: Activation period: MDA reaction starts with an activation period, which corresponds to the in-situ generation of the active phase at the beginning of the reaction in the presence of methane. Experiments were carried out for different contact times ranging from 0.19 s to

2.04 s, obtained by varying the catalyst mass and keeping the flow rate constant (**Figure 2b**). Independent of the contact time, no product is formed during the activation period. Yet, its duration is proportional to the contact time (**Figure 2c**) and the amount of molybdenum oxide in the catalyst bed. This proportionality suggests a stoichiometry reaction between methane and molybdenum species.

Several experimental studies have been published so far, which all highlight the formation of the molybdenum carbides (Mo_xC_y) and/or oxy-carbides ($Mo_xC_yO_z$). [42,7] Recently, a precise structure of the active phase for MDA reaction on Mo/ZSM-5 catalyst has been refined through a systematic theoretical investigation by the group of E. Pidko. [37] In particular, the authors investigated the possible reaction paths toward the reduced molybdenum (oxy)carbide species during the activation of Mo/ZSM-5 by means ab initio thermodynamic calculations, used for computing the chemical potential μ_{CH_4}, μ_{H_2} and μ_{CO} for all intermediates occurring during the reduction of supported Mo_2O_5 to the MDA active phase consistent with supported Moieties. Following these findings the energies of all elementary reactions of C/O exchange in the presence of methane were modelled. The obtained results are represented **in Scheme 3**. All the reactions involved in the carburation process are endothermic. The enthalpy of the reduction of Mo_2O_5 to Mo_2C_2 is very high, i.e, 26.6 eV. Considering the reaction conditions, which feature the highest methane chemical potential, μ_{CH_4}, while the partial pressure of the products CO, H_2O and H_2 are clore to zero under the applied dynamic flow. Following the Chatelier principal, the energetically favorable compound is the carbide Mo_2C_2.

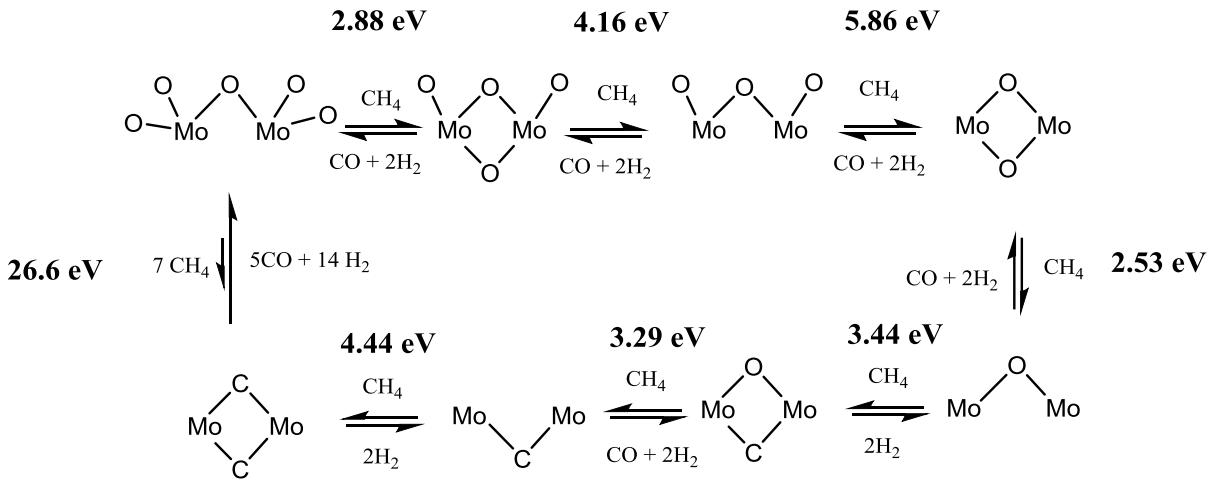

Scheme 3. O/C exchange on Mo_2O_5 species and computed enthalpies for each step.

During the activation period, the methane conversion remains constant at 25 %. **Figure 2b** clearly shows that the activation time ($t_{activation}$) is directly related to the contact time. The amount of CH_4 which reacts with the molybdate oxides is proportional to the amount of molybdenum present in the catalyst bed, i.e., ≈ 2 moles of Mo react with 1 mole of CH_4. (**Figure 3**). The carburation occurs on both MoO_3 oxide phase segregated outside the channels [15, 43, 44] and the supported Mo_2O_5 dimers anchored within the zeolite channels by bridging two Al centers as visible in equations 5 and 6, respectively.

$$4\,MoO_3 + 7\,CH_4 \rightarrow 2\,Mo_2C + 3\,CO_2 + 2\,CO + 10\,H_2 + 4\,H_2O \qquad \text{(eq. 5)}$$

$$Mo_2O_5 + 7\,CH_4 \rightarrow Mo_2C_2 + 5\,CO + 14\,H_2 \qquad \text{(eq. 6)}$$

Taking into account the proportion of MoO_3 and Mo_2O_5 (80/20) with the stoichiometry coefficients of equations 5 and 6 (7/4 and 7/2), the theoretical amount of methane that should react with the molybdenum is : $\frac{7}{4} \times 0.80 + \frac{7}{2} \times 0.20 = 2.0$, which is in good agreement with the proportions found experimentally (**Figure 3**).

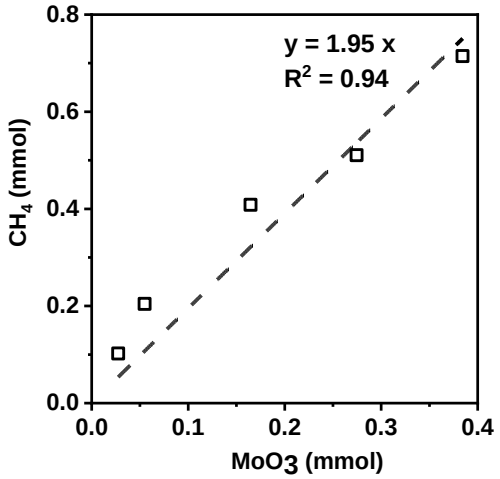

Figure 3: Amount of reacted methane during the activation period as a function of the molybdenum oxide in the catalytic bed.

It should be pointed out that the absence of benzene during the activation period means that carburization occurs at the same time over the entire catalytic bed. In our operating condition, the kinetic rate of carburation of the Mo/H-ZSM-5 catalyst is 0.027 mmol of MoO_3 converted per min. Therefore, carburation appears to be a relatively slow step.

Step 2: Induction period. Once the molybdenum oxide is entirely reduced to carbide, there is a concomitant and significant increase of ethylene (m/z = 27), benzene (78), toluene (92), and naphthalene (128) in the gas phase (**Figure 2b and** see Supporting Information **Figure S2**). It is worth mentioning that the time required to reach the maximum ($t_{induction} = \mathrm{t_{max}} - \mathrm{t_{activation}}$) increases proportionally with the contact time (**Figure 2b**). This duration is much longer than the activation period and is defined in the literature as induction period. [45]

The activation of the first CH_4 on Mo_2C_2 species at 6 MR-δ position was investigated through theoretical modeling. The first step of the MDA reaction is consistent with methane activation, leading to breaking a C-H bond and forming a C-C bond. Once the Mo_2C_2 active site is formed, the methane activation is fast and efficient. Indeed, the activation energy is E_a = 0.8 eV leading to the formation of one Mo-H species and a bridging C-CH_3. The formation of

the C-C and Mo-H bonds compensates for the breaking of the C-H bonds. (**Figure 4**). The desorbed ethylene reacts on the zeolite Brønsted acid sites and yields aromatics.

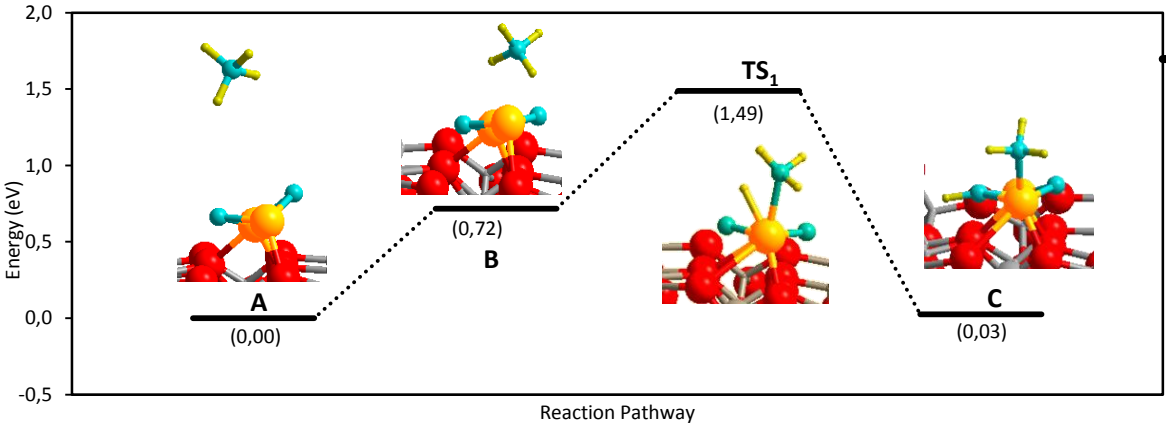

Figure 4: Reaction mechanism for diffusion into zeolite and activation of the first CH_4 for the catalytic MDA reaction on $[Mo_2C_2]^{2+}$ system at 700 °C

Figure 5 shows, as a function of the contact time (τ), after 0.5 h of reaction, the methane conversion, the formation rate of hydrogen, and the mass yields of ethylene, benzene, toluene, and naphthalene. The time of 0.5 h corresponds to the duration of one GC analysis. The methane conversion increases with the contact time until reaching a plateau corresponding to the expected thermodynamic equilibrium at 700 °C, i.e., 12.5% [4] (**Figure 5a**). Such trend was reported recently by Bhan et al. [46] Yet, by carrying out the reaction at lower contact time than these previously recorded in the open literature, it is possible to emphasized the increase is not proportional to τ and follows an S-shaped function. A similar shape is observed for the benzene, toluene, and naphthalene yields as a function of τ (**Figure 5d, e, and f**). The ethylene yield and the hydrogen formation rate are initially proportional to τ. Then the first one passes through a maximum at 0.25 s (**Figure 5c**), while the second one approaches steady-state formation (**Figure 5b**).

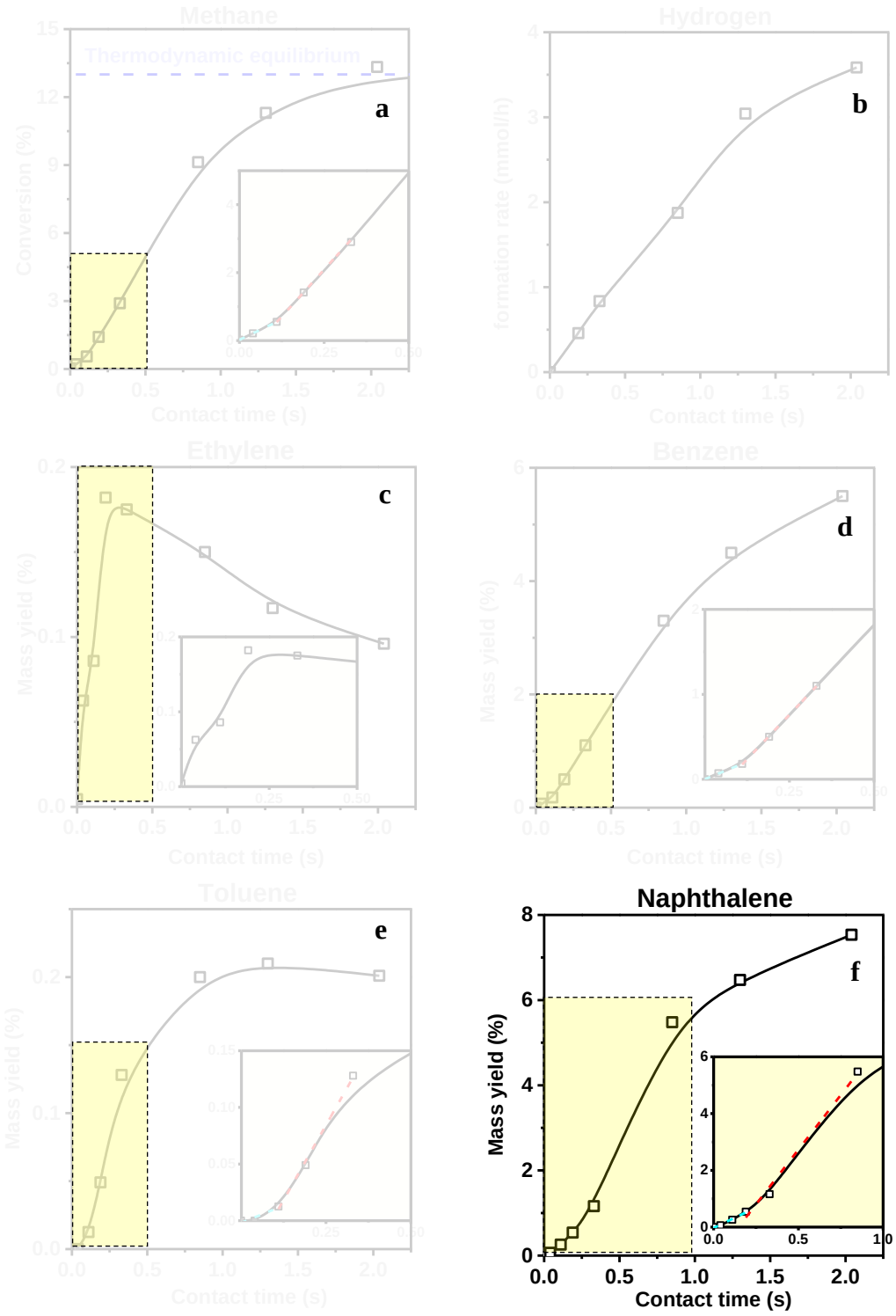

Figure 5:(a) Initial molar conversion of methane, (b) formation rate of hydrogen, mass yields of (c) ethylene, (d) benzene, (e) toluene, and (f) naphthalene as a function of contact time. The yellow square is a zoomed area at the lower contact times.

Magnification at short contact times allows for determining two kinetic rates for the methane conversion. The first one (blue: k_1) is assigned to the methane conversion rate at short residence times (<0.11 s), whereas the second (red: k_2) is attributed to the conversion rate at long contact times (> 0.11 s). The quantification of these kinetic data leads to $k_2 \sim 2*k_1$, which evidences that the rate rises rapidly with increasing residence time. These results indicated that methane is initially slowly transformed into aromatics. Thereafter, methane conversion accelerates and aromatics production increases. For this reason, the major formation of aromatic compounds occurs as a result of secondary reactions.

S-shaped curves are typical features for reactions with autocatalytic kinetics. Such phenomenon is already well documented for the methanol to olefin process (MTO). [47, 48] MTO has been widely investigated, and the involvement of an organocatalytic intermediate identified as hydocarbon pool (HCP) could be evidenced. Methanol reacts with the active hydrocarbon pool species to produce light olefins, which are further transformed by condensation, alkylation, cyclization, and hydrogen transfer reactions to produce higher olefins, alkanes, and aromatic hydrocarbons. [49] The observation of an active role of the HCP in the MDA reaction[9 21] allows us to assume that these entities play a critical role in the MDA process. The generation of the HCP could occur during the induction step.

More recently, our study on ethylene dehydroaromatization (EDA) in harsh conditions [50]: atmospheric pressure, 700 °C with a ethylene partial pressure of 0.05 (5 mol% in N_2) over a H-ZSM-5 (Si/Al = 40) exhibits the same behavior: an induction period followed by deactivation. The same trend was also observed by Vollmer et al. [51] The aromatics yield increases during the latter stage, despite a significant loss of the acid site concentration resulting from coking. This induction period corresponds to the formation of HCP species composed of 2 to 5 aromatic cycles. [50] The kinetic study revealed that the developing HCP species are two times more active than Brønsted acid sites in the fresh zeolite. The mechanism of ethylene dimerization occurs on HCP through a succession of alkylation and pairing reactions, while on Brønsted acid sites dimerization is induced via an unstable

primary carbenium ion (**Scheme 4**). Therefore, ethylene dimerization is faster on HCP than on proton sites. Moreover, these results suggest that in methane dehydroaromatization, the rate-limiting step is the dimerization of ethylene.

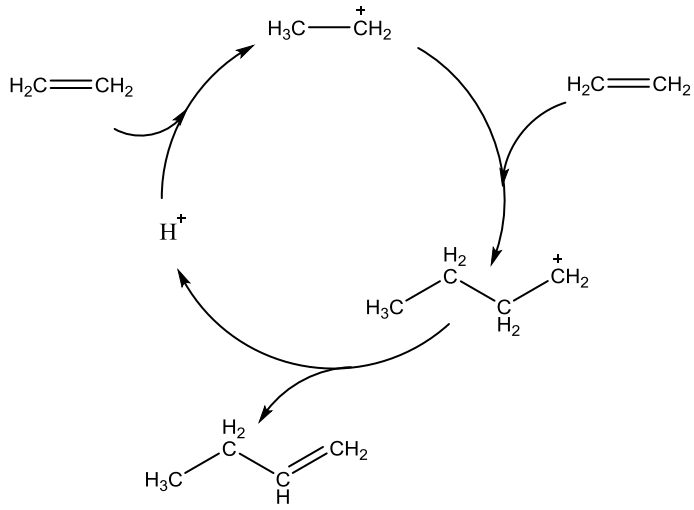

Scheme 4: Ethylene dimerization on protonic sites.

Step 3. Deactivation period. **Figure 6** shows the methane conversion and the formation rate of hydrogen obtained at different contact times as a function of the time-on-stream. The rate of deactivation depends on the contact time. An exponential function was assumed for catalyst deactivation, depending on the deactivation constant (k_d) and the time-on-stream.[52] The constant deactivation is fitted to the experimental data of the methane conversion ($k_d^{methane}$) and formation rate of hydrogen $\left(k_d^{hydrogen}\right)$. The two deactivation constants are plotted as a function of the contact time (**Figure 6b**). The obtained values compare well, suggesting that the deactivation of hydrogen follows that of methane, which fosters the concept that hydrogen production is directly related to methane conversion. Furthermore, higher contact times lead to increased activity and, surprisingly to higher stability.

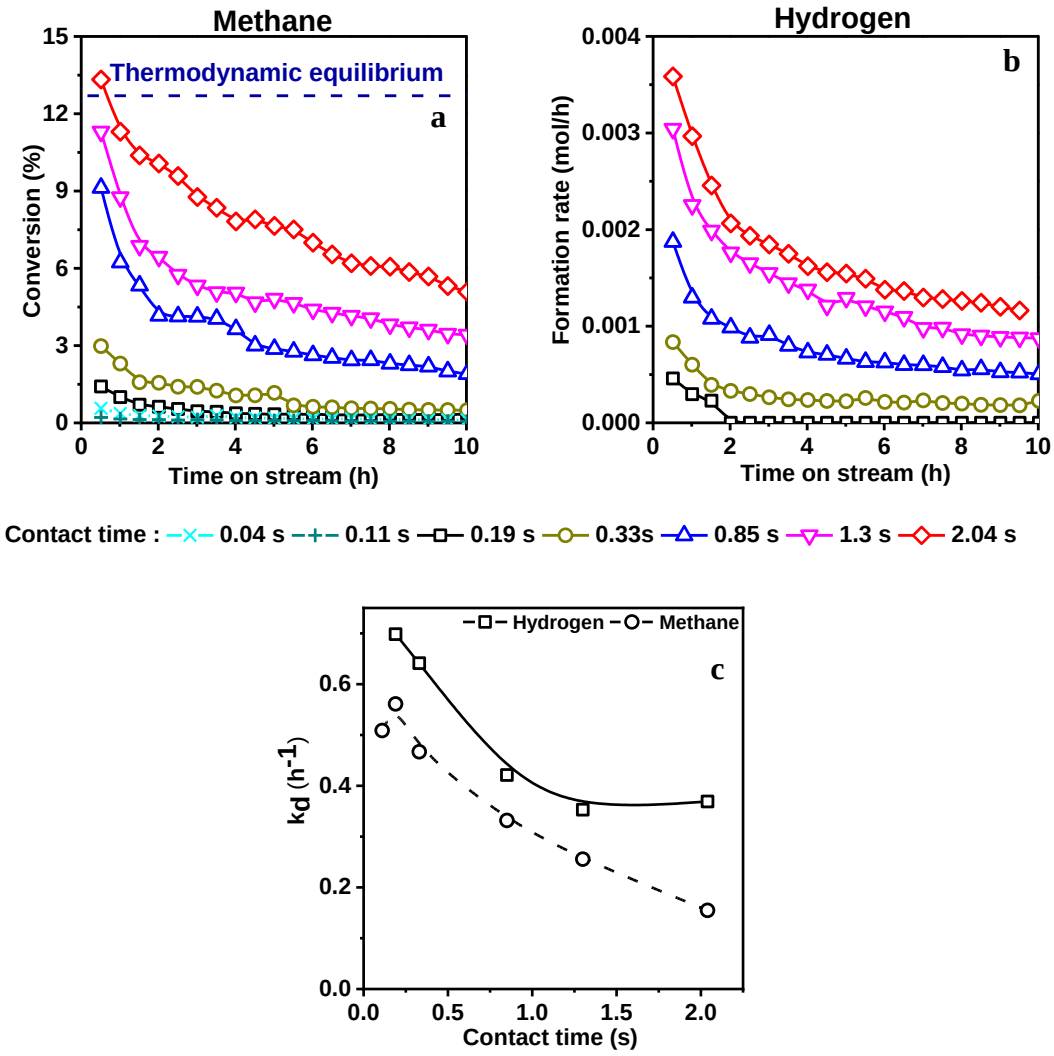

Figure 6: (a) Molar conversion of methane, (b) hydrogen formation rate and corresponding (c) deactivation constant as a function of time on steam for different contact time.

Figure 7 displays, as a function of methane conversion (X_{CH4}), the formation rate of hydrogen and ethylene, benzene, toluene, naphthalene mass yields obtained for different contact times. For each contact time, the highest conversion corresponds to the initial product yields (at 0.5 h), while the lowest conversion values correspond to those obtained on the spent catalyst after 10 h of reaction. Ethylene and hydrogen are primary products; benzene appears as an apparent primary product. Toluene and naphthalene are formed at very low conversion, less than 0.5%, and must be considered apparent secondary products. The benzene, naphthalene, and hydrogen yields increase with conversion. Those of ethylene

and toluene pass through a maximum. Thus, ethylene is rapidly converted into aromatics, while toluene may undergo a dealkylation reaction. This apparent reaction scheme (**Scheme 5**) suggests that the formation rate of aromatics is much faster than that of ethylene.

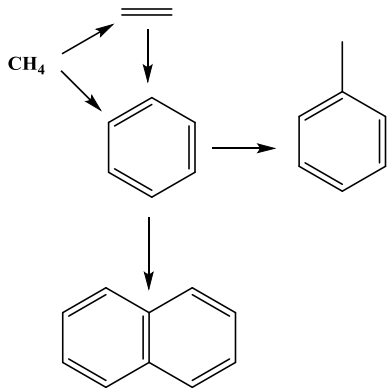

Scheme 5: Apparent reaction scheme of the MDA reaction.

Recently, the group of Bhan et al. [46] identified the exact same correlation between methane conversion and products selectivity pointing out the non-selective deactivation step. Indeed, by varying the contact time, the wide range of formed hydrocarbons concentration and methane conversion, the data remain identical throughout the deactivation step. They also proposed an apparent reaction scheme in which the molybdenum carbide is the only relevant active site of the reaction. Benzene also appears to be formed rapidly after ethylene production.

A slight selectivity change can be observed in **Figure 7**. Indeed, for higher contact times, naphthalene selectivity decreases, whilst benzene selectivity increases. This difference might be related to the produced hydrogen, especially at high conversion, promoting benzene desorption and inhibiting naphthalene formation.

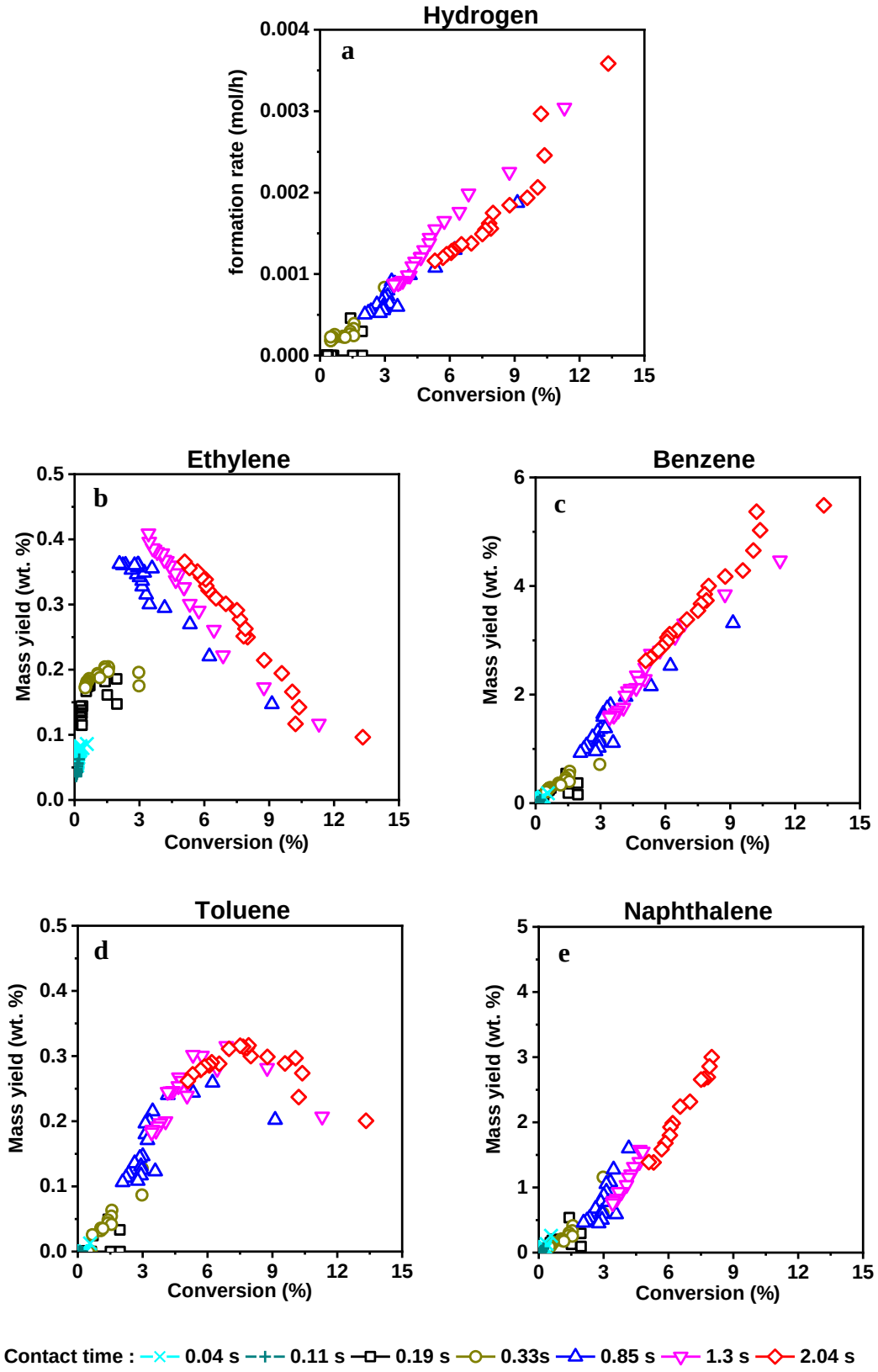

Figure 7: (a) Formation rate of hydrogen, mass yields of (b) ethylene, (c) benzene, (d) toluene, (e) naphthalene as a function of the methane conversion for different contact time.

3.3. Characterization of the spent catalyst and deactivating species

Thermogravimetric analyses followed by mass spectroscopy were performed to study the combustion of coke species on the catalysts after 10 hours of reaction. Independent of the contact time, the combustion profiles are similar and feature three distinct parts. A slight weight gain appears from ~ 350 °C to 450 °C, followed by a first weight loss up to 520 °C and a second weight loss up to 620 °C (**Figure 8a**). The weight gain corresponds to the oxidation of the

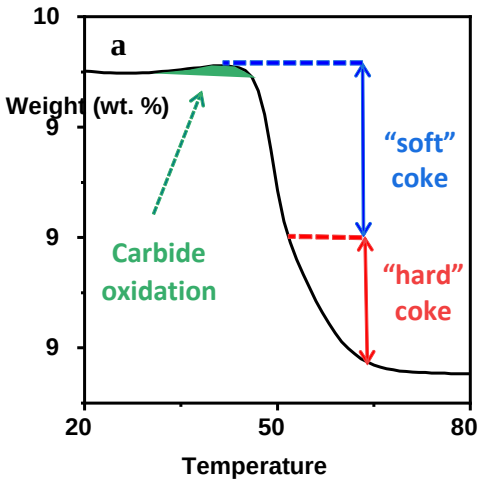

carbides (Mo_2C).

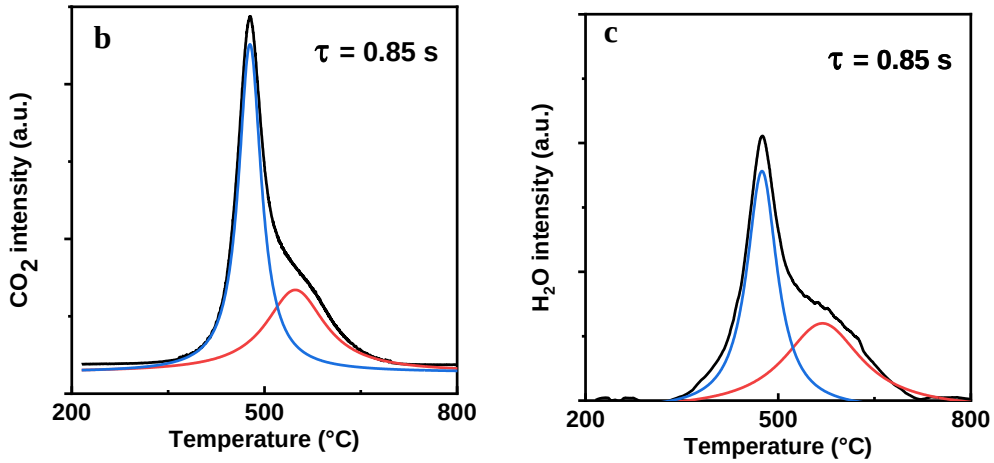

Figure 8: (a) Example of thermogravimetric analysis of a spent catalyst Sp/0.85 with associated (b) CO_2 and (c) H_2O profiles, deconvoluted into two peaks: in blue, "soft" coke, and in red, "hard" coke.

The two losses in TGA are more evident with the mass signal of the oxidation products, i.e., CO_2 (m/z= 44) and H_2O (m/z= 18). (**Figures 8b and 8c**). Independent of the selected mass-to-charge ratios, the combustion profiles can be deconvoluted into two well-defined peaks. The first and second peaks are frequently attributed to the oxidation of "soft" (S) and "hard" (H) coke, respectively. [28] The total mass loss corresponds to the coke content (T), and the amounts of S and H coke are calculated from the surfaces of the deconvoluted peaks.

Figure 9 reports the total "soft" and "hard" coke content and weight gain as function of the contact time. Considering that only Mo_2C is present on the external surface, estimating the

molar percentage of molybdenum carbide that oxidizes before coke combustion is possible. Indeed, the Mo_2C oxidation leads to a theoretical mass increase of 41% (**eq.7**), a value confirmed experimentally with commercial Mo_2C (purity = 99.5%) (see Supporting Information **Figure S3**).

$$Mo_2C + 4\,O_2 \longrightarrow 2\,MoO_3 + CO_2 \qquad (+40\%\ in\ mass) \qquad \text{(eq.7)}$$

From the mass gain (**Figure 9b**), between 4 and 10% of Mo_2C can be oxidized. Surprisingly, increasing the contact time leads to a more significant amount of produced hydrogen and Mo_2C with higher stability towards oxidation. This result suggests that either one part of the Mo_2C is oxidized into oxide or further MoC_x, where x is ~ 3.6, species are present on the external surface, depending on the residence time.

As far as the coke combustion is concerned, the total and “hard” coke contents decrease, while that of the “soft” one remains constant (ca 3.2 wt.%) as the contact time increases (**Figure 9a**). On the catalysts that operated with the longest contact time (Sp/2.04, **Table S1**), the coke is almost exclusively composed of “soft” coke, while with the shortest (Sp/0.11), the proportion of both types of coke is similar.

Coke deposition has a stronger impact on the concentration of Brønsted acid sites than on micropore volume. The deposition of 4 wt.% of coke reduces to more than 75% BAS and only 20% of V_{micro} (see Supporting Information **Figure S4**). The toxicity of the “soft” coke is limited, as the deactivation constant (k_d) is independent of its amount, which allows its qualification as a spectator (**Figure 9c**). In contrast, the deactivation constant is directly related to the “hard” coke content (**Figure 9d**).

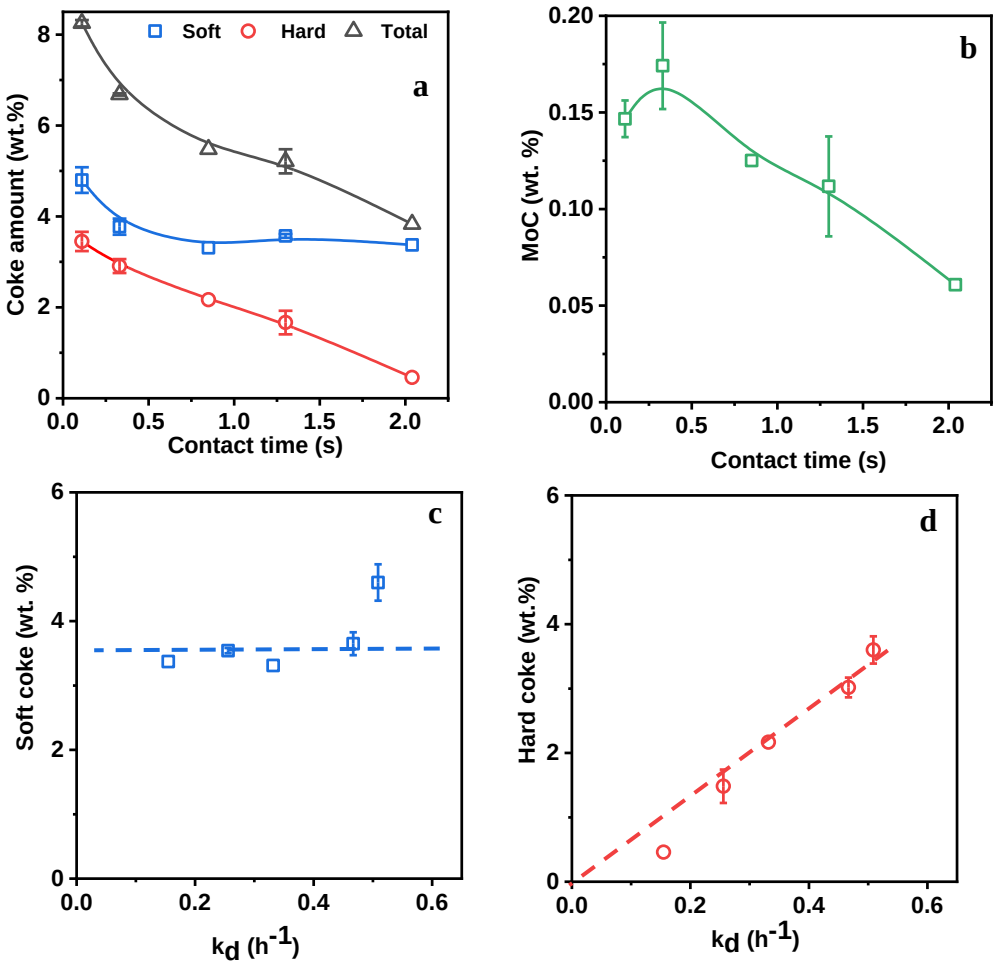

Figure 9: (a) Total, "soft", and "hard" coke contents and (b) weight gain as a function of contact time. (c) "Soft" and (d) "hard" coke contents vs. deactivation constant (k_d)

The formation of coke appears to be rather unusual, as contact time enhancement usually mitigates coke deposition (**Figure 9**).[53] Thus, coking should be much faster at long contact times with high temperatures because of the high coke precursor concentration. In contrast, the coking rate should be relatively slow for low residence times, and deactivation should be mainly due to acid-site poisoning. [53] To confirm this particular bahavior we carried out additional elemental analysis presented in **Figure S5**. The direct relation with a slope of ~ 1 supports the coke amount recovered on the spent samples.

As the deactivation mechanism remains still unclear, the catalyst deactivation (step 3) results from complex pathways. Its rate depends on the amount of produced hydrogen, as the total coke content decreases with the amount of produced hydrogen (see Supporting Information

Figure S7). Thus, adding low partial hydrogen pressure to the methane feed allowed reaching improved catalytic stability and lower coke contents. [26] [54] However, it has the substantial drawback of shifting the thermodynamic equilibrium towards the methane side, which negatively impacts conversion. In addition, numerous studies [55] on the use of H_2 permeable membranes revealed that, even if the hydrogen removal increases the methane conversion and aromatics formation rate, it favors coke accumulation on the catalyst. [56] Notably, Larachi et al. demonstrated that native hydrogen reactivates the catalyst by removing coke-type carbon. Indeed, operating in starved hydrogen flow enables accelerating the establishment of non-carbidic carbon deposited on top of the molybdenum carbide, which migrated on the external zeolite surface. [57]

The produced hydrogen has no impact on the "soft" coke (**Figure 9**) formation rate. Indeed, independently of the amount of produced hydrogen (**Figure 5**), its content remains stable. The autogenous hydrogen prevents the formation of "hard" coke, which causes deactivation. By contrast, "soft" coke is an active center for the transformation of ethylene by a hydrocarbon pool mechanism formed during the induction period (step 2). The number of carbon atoms constituting the HCP can be assessed from the concentration of neutralized Brønsted acid sites by assuming a ratio of one molecule of "soft" coke per poisoned acid site (plausible hypothesis due to the limited loss of micropore volume, (see Supporting Information **Figure S4**), (

$$[wt.\%\ C]_{soft} = 12 \times\ n_c^{nt} \times ([\mathrm{H}^+]_0 - [\mathrm{H}^+]_\mathrm{i}) \qquad \text{(eq.8)}$$

n_c^{nt}: carbon molar quantity in the non-toxic coke per amount of catalyst

$H_0^+ - H_i^+$: number of neutralized Brønsted acid sites

HCP is constituted of 20 carbon atoms per molecule of coke, which could correspond to coke molecules that classical form in ZSM-5 such as pyrene (d= 1.27 g cm^{-3}) and/or benzopyrene (d= 1.24 g cm^{-3}). [58] This hypothesis is consistent with the composition of the molecular coke formed during the dehydroaromatization of ethylene on HZSM-5 at 700 °C. Indeed, coke analysis has shown that the molecules trapped within the zeolite micropores during the

induction period are composed of anthracene, phenanthrene, pyrene, and benzo(e)pyrene. [50] It is essential to remind that coke growth occurs following a genuine shape-selective mechanism. [59] Hence, by considering that "soft" coke should feature an assumed density of 1.3 g cm^{-3}, the apparently occupied volume by this coke on the spent catalyst having almost exclusively this type of coke should be 0.02 g cm^{-3}, which is consistent with the residual micropore volume in the spent catalysts. Additionnaly, the calculated molar ratio H/C of the total coke based on elemental analysis is ~ 0.6, which is consistent with polyaromatic compounds previously proposed. The high contact presents very low amount of "hard" coke so we can assume the "soft" coke is composed of polyaromatic compounds inside the zeolite channel

Regarding the toxic coke ("hard" coke), comparable calculations were completed to establish its possible nature. We assume that the higher deactivation rate refers to all carbide species at 6 MR-δ position and external surface (3.1 wt. %) that interact with "hard" coke. Equation 9 allows determining the number of carbon adsorbed on one molybdenum atom for each spent catalyst (see Supporting Information **Table S1**)

$$\frac{C}{Mo}(i) \approx \frac{n_c^t}{n_{Mo}} * \ 0.51/k_d^{methane}(i) \qquad \text{(eq. 9)}$$

n_c^t : molar quantity of the carbon in toxic coke per amount of catalyst

n_{Mo} : molybdenum molar quantity per amount of catalyst

It should be noted that once the catalyst is totally deactivated (i.e., methane conversion is <1 %), the C/Mo value reaches ~ 8. (**Figure 10**). This ratio implies that the toxic coke could be due to strongly adsorbed products, indicating that the deactivation could result from a strong inhibitory effect of the product molecules, i.e., benzene (n_C=6) and naphthalene (n_C=10). This assumption is consistent with the higher hydrogen content of "hard" coke compared to "soft" coke (see Supporting Information **Figure S6**). In addition, the inhibition could be mitigated by the produced hydrogen.

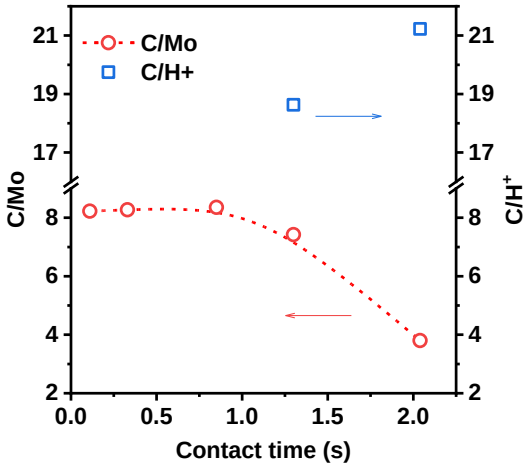

Figure 10: Evolution vs. contact time of the nature of the "soft" and "hard" coke characterized by the molar ratios of C/H^+ and C/Mo, respectively

To confirm these results, regeneration of the spent catalyst Sp/2.04 was performed and monitored by operando Raman. The Raman spectrum of as-received spent catalyst at 30°C shows two broad lines at 1350 and 1595 cm^{-1}, referring to the so-called ***D*** and ***G*** bands in graphite-based materials, and presently assigned to polyaromatic hydrocarbon species. [60] No scattered signal is detected in the 600-1100 cm^{-1} range (**Figure S8**) confirming that both zeolite- supported oxomolybdate phase and the MoO_3 crystals have reacted in the course of the MDA reaction. Upon heating under dry O_2/He flow, the intensities of both peaks detected at 1350 and 1595 cm-1 are mostly stable up to 300°C. Between 350°C and 500°C, the intensities of both peaks markedly decrease with a maximal rate detected in the 450-500°C range, as evidenced by the derivative curves shown in **Figure 11.a**. Such a decrease is real-time correlated to a marked increase of CO_2 production at 480°C, thus confirming that the as observed carbon deposit has been removed from the powder by oxidation and desorption from the zeolite surface. At 550°C, although the Raman signature of carbon deposit is not detected anymore, another significant maximum of CO_2 production is reached. In other words, the CO_2 produced at 550°C is corresponding to the reaction and desorption of a carbon species which was not detected by means of Raman spectroscopy. Interestingly, no feature related to Mo oxide has been detected at end of the TPO (700°C). This may be due to the strong contribution from visible-range fluorescence which occurred as the temperature

exceeded 600°C. The temperature-controlled profile of CO_2 production measured using the Raman operando set-up is in fine agreement with the one obtained from the thermogravimetric analysis shown in **Figure 8**. A coupling of results can thus be made for establishing the experimental evidence that the so-called soft coke is genuinely consistent with polyaromatic hydrocarbons which plausibly form the HCP. On the other hand, the *hard coke* is consistent with moieties undetectable to visible Raman spectroscopy run in the present conditions.

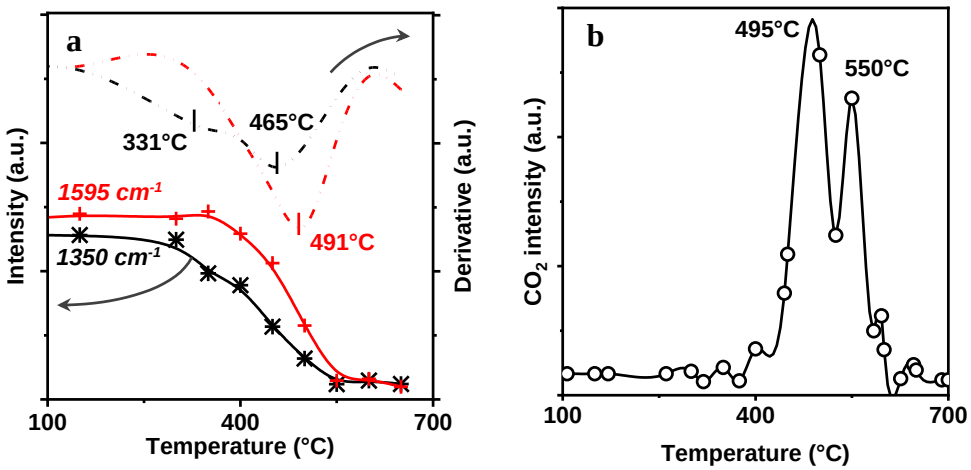

Figure 11: (a) Analysis of both 1350 (black) and 1595 cm^{-1} (red) Raman peaks - typical of polyaromatic hydrocarbons- recorded along the TPO of the spent catalyst Sp/2.04: evolution of peak area as a function of temperature (plain lines) and corresponding derivative (dot-dashed lines). (b) CO_2 production measured online -simultaneously to the collection of Raman spectra shown in (a). The lines are drawn simply to guide the eyes

DFT modeling has been used to compute the adsorption energies of both species presumed to act as “hard coke” (benzene and naphthalene) on the Mo_2C_2 active site to confirm their plausibility for active phase poisoning. The as-afforded relaxed adsorption structures are given in Erreur ! Source du renvoi introuvable.**S1,** together with the corresponding calculated adsorption energies. Our calculations show that the adsorption of naphthalene on the supported Mo_2C_2 site results in a stable structure with adsorption energy of -0.65 eV, confirming that naphthalene can block the active site and causes catalyst deactivation. The adsorption of benzene is further feasible on the Mo_2C_2 site, featuring a similar adsorption energy of -0.78 eV (**Figure 12**).

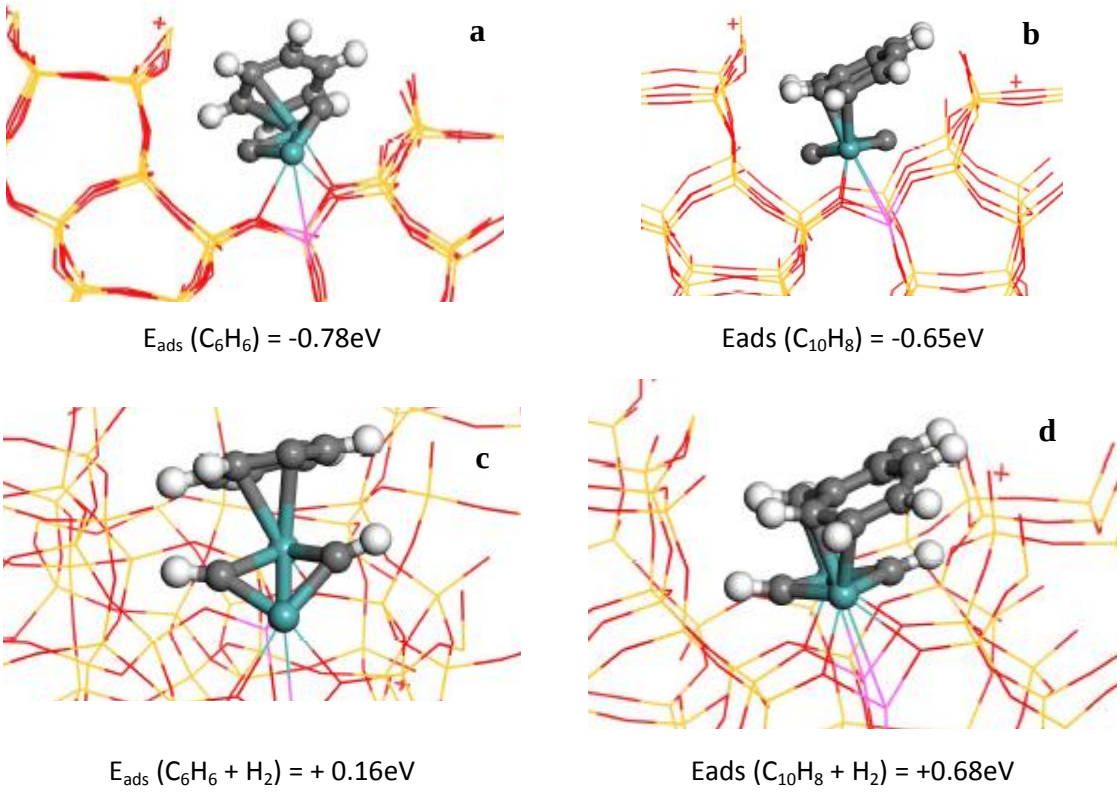

E_{ads} (C_6H_6) = -0.78eV

Eads ($C_{10}H_8$) = -0.65eV

E_{ads} (C_6H_6 + H_2) = + 0.16eV

Eads ($C_{10}H_8$ + H_2) = +0.68eV

Figure 12: Computed structures of (a) benzene, (b) naphthalene, (c) benzene co-adsorption H_2 and (d) naphthalene co-adsorbed H_2 adsorbed at Mo_2C_2 active site located at δ-channels of ZSM-5 and corresponding adsorption energies.

Upon co-adsorbing benzene with H_2, the adsorption energy reduces from -0.78 down to 0.16 eV (**Figure 12**), indicating that H_2 inhibits benzene adsorption to the active site. The key role of H_2 is even more emphatized as the calculated adsorption energy reaches 0.68 eV upon co-adsorbing naphthalene with H_2. Thus, in the catalyst deactivation, the mitigating role of H_2 is indeed observed experimentally.

Kosinov et al widely discussed coke nature recovered on the spent samples in a well-notable paper. [21] Briefly the apparent difference observable in TG profiles results only from the diffusion limited combustion inside the pore. There is no coke chemical difference between the "soft" coke and "hard" since ^{13}C NMR analysis show only sp^2 type of coke. Thus they concluded the fraction of "hard" coke correspond to polyaromatic compounds trapped within the zeolite channel, whereas we proposed here the opposite: the "soft" coke is in fact the polyaromatic compounds anchored on BAS inside the zeolite channel.

We liked to raise the possibility that this change of interpretation depends on the combustion profiles. Indeed, we obtained a contribution of “soft” coke predominant, whereas the team of Kosinov presents a contribution of “hard” coke more important. This change of behavior is related of the textural properties of the material (Mo content, Si/Al molar ratio, crystal size,…).

Then, the proposed coke natures are in good agreement with the sp^2 hybridized C atoms. It is crucial to mention the coke formation follows a genuinre shape-selectivity reaction. Thus, a low coke amount (5-6 wt.%), recovered on the spent samples with a slight reduction of the microporous volume (~ 20%) of a tri dimensionnal zeolite will apparently not induce oxygen diffusion limitation. [59] [61]

From all the results presented in the open literature [21] [26] [14], we think the higher contribution in the TPO profile is probably due to the internal coke wheter the coke type it is.

Finally it should be noticed, the active species inhibition by aromatic compounds appears under specific conditions, i.e low contact time thus very small amount of autogenous hydrogen. At higher contact time under the traditional MDA experimental conditions, the hydrogen formation is sufficient to desorb the aromatic compounds from the active species.

Conclusion and Outlook

Dehydroaromatization of methane over a Mo/H-ZSM-5 catalyst involves the constant evolution of the molybdenum species from preparation and throughout the catalyst lifetime**.** **Scheme 6** summarizes the evolution of the Mo species of the four stages: calcination-pretreatment (0), activation (1), induction (2), and deactivation (3) (the regeneration stage is not addressed in this study).

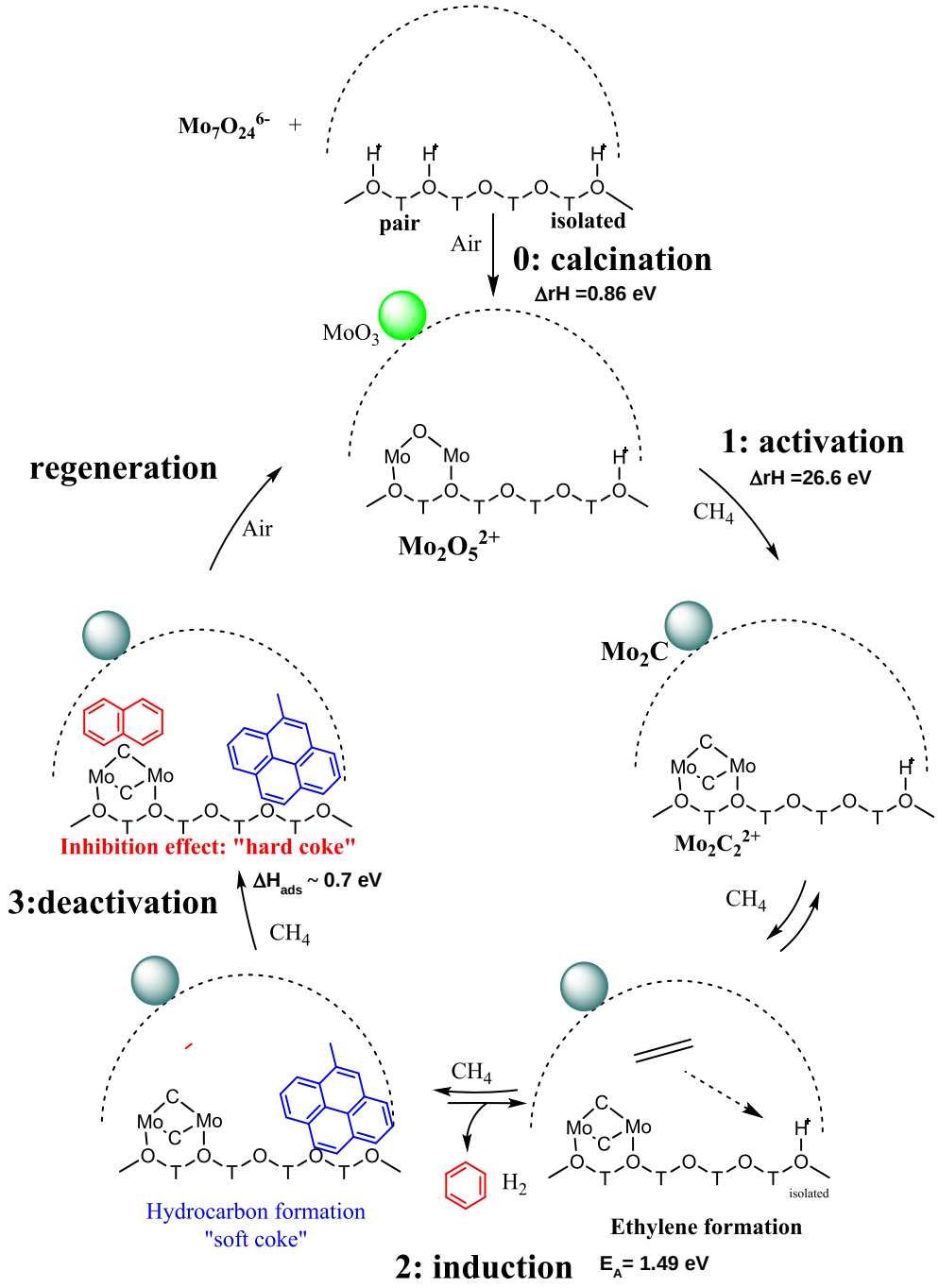

Scheme 6. Mechanisms involved in the four steps of the methane dehydroaromatization reaction.

During the calcination (step 0) of H-ZSM-5 impregnated with $(NH_4)_6Mo_7O_{24}.4H_2O$, a part of the developed oxide (MoO_3) reacts stoichiometrically with the bridged hydroxyl group pairs to give dimeric $[Mo_2O_5]^{2+}$ entities (**step 1**). This solid-solid reaction is energetically favorable

and amounts to 0.85 eV. As the number of aluminum pair sites is limited, an important portion of the molybdenum (80%) remains located on the external surface as MoO_3.

MoO_3 and $[Mo_2O_5]^{2+}$ react stoichiometrically with methane and are reduced into MoC_2 and $(Mo_2C_2)^{2+}$ cation, respectively. This reduction phase is called the activation period (step 1). The carburization reaction of the oxomolybdate cation anchored in zeolite is highly endothermic (26.6 eV). However, since the chemical potential of CO and H_2 is close to zero, the reaction equilibrium is shifted to the formation of carbide species.

After the activation period, characterized by the absence of aromatics formation, the generated carbide species anchored within the zeolite activates methane leading to desorbed products (Step 2: induction period). Mo_2C is a spectator species. Methane activation energy on $Mo_2C_2^{2+}$ is 1.49 eV. During the first stage of the induction step, ethylene dimerizes on the acidic Brønsted sites. Then is easily transformed into benzene and polycondensed aromatic compounds, which are composed of 20 carbon atoms (pyrene, methyl-benzopyrene). The latter, named “soft” coke, does not poison active sites as they allow the transformation of ethylene two times faster than the proton sites and was identified to act as HCP. In methane dehydroaromatization, the rate-limiting step is the dimerization of ethylene.

Deactivation (step 3) depends on the contact time and decreases with an increasing amount of produced hydrogen. H_2 acts as a catalyst surface scavenger by promoting the desorption of aromatic compounds that strongly adsorb on carbide species. The introduction of hydrogen into the feed gas shifts the thermodynamic equilibrium towards decreased conversion. Deactivation is not related to pore blocking but rather to “poisoning” by “hard” coke, which is composed of hydrogenated and lighter molecules than “soft” coke. Hence, deactivation results from strong adsorption of aromatics on $Mo_2C_2^{2+}$, with adsorption exceeding 0.7 eV.

The main challenge in methane activation is the adequate preparation of the $Mo_2C_2^{2+}$ active phase. Therefore fine-tuning the Si/Al ratio is mandatory. The addition of promoters on the catalyst (Pt, W) or to the gas feed (CO, CO_2) should not improve the methane C-H activation but could limit catalyst deactivation by favoring aromatics desorption.

Acknowledgments: The authors acknowledge financial support from the European Union (ERDF) and “Région Nouvelle Aquitaine”.

A. Beuque, H. Hao**,** A. Sachse, E. Berrier, J.P. Paul, N. Batalha, and L. Pinard thank the European Union’s Horizon 2020 research and innovation program for its funding under grant agreement No 814548. This publication only reflects the author’s views, and neither Agency nor the Commission is responsible for any use that may be made of the information contained therein.

References:

(1) Huang, K.; Maravelias, C. T. Synthesis and Analysis of Nonoxidative Methane Aromatization Strategies. *Energy Technology* **2019**, *n/a* (n/a), 1–11. https://doi.org/10.1002/ente.201900650.

(2) Tang, P.; Zhu, Q.; Wu, Z.; Ma, D. Methane Activation: The Past and Future. *Energy Environ. Sci.* **2014**, *7* (8), 2580–2591. https://doi.org/10.1039/C4EE00604F.

(3) Wang, L.; Tao, L.; Xie, M.; Xu, G.; Huang, J.; Xu, Y. Dehydrogenation and Aromatization of Methane under Non-Oxidizing Conditions. *Catal Lett* **1993**, *21* (1–2), 35–41. https://doi.org/10.1007/BF00767368.

(4) Zhang, Z.-G. Process, Reactor and Catalyst Design: Towards Application of Direct Conversion of Methane to Aromatics under Nonoxidative Conditions. *Carbon Resources Conversion* **2019**, *2* (3), 157–174. https://doi.org/10.1016/j.crcon.2019.07.001.

(5) Clatworthy, E. B.; Konnov, S. V.; Dubray, F.; Nesterenko, N.; Gilson, J.-P.; Mintova, S. Emphasis on the Properties of Metal-Containing Zeolites Operating Outside the Comfort Zone of Current Heterogeneous Catalytic Reactions. *Angewandte Chemie n/a* (n/a). https://doi.org/10.1002/ange.202005498.

(6) Ma, S.; Guo, X.; Zhao, L.; Scott, S.; Bao, X. Recent Progress in Methane Dehydroaromatization: From Laboratory Curiosities to Promising Technology. *Journal of Energy Chemistry* **2013**, *22* (1), 1–20. https://doi.org/10.1016/S2095-4956(13)60001-7.

(7) R. Ismagilov, Z.; V. Matus, E.; T. Tsikoza, L. Direct Conversion of Methane on Mo /ZSM-5 Catalysts to Produce Benzene and Hydrogen : Achievements and Perspectives. *Energy & Environmental Science* **2008**, *1* (5), 526–541. https://doi.org/10.1039/B810981H.

(8) Vollmer, I.; Kosinov, N.; Szécsényi, Á.; Li, G.; Yarulina, I.; Abou-Hamad, E.; Gurinov, A.; Ould-Chikh, S.; Aguilar-Tapia, A.; Hazemann, J.-L.; et al. A Site-Sensitive Quasi-in Situ Strategy to Characterize Mo/HZSM-5 during Activation. *Journal of Catalysis* **2019**, *370*, 321–331. https://doi.org/10.1016/j.jcat.2019.01.013.

(9) Kosinov, N.; Hensen, E. J. M.; Uslamin, E. A. Confined Carbon Mediating Dehydroaromatization of Methane over Mo/ZSM-5. *Angewandte Chemie International Edition* **2018**, *57* (4), 1016–1020.
(10) Tan, P. L.; Leung, Y. L.; Lai, S. Y. The Effect of Calcination Temperature on the Catalytic Performance of 2 Wt.% Mo/HZSM-5 in Methane Aromatization. *Applied Catalysis A: General* **2002**, *228*, 115–125. https://doi.org/10.1016/S0926-860X(01)00955-3.
(11) Borry, R. W.; Kim, Y. H.; Huffsmith, A.; Reimer, J. A.; Iglesia, E. Structure and Density of Mo and Acid Sites in Mo-Exchanged H-ZSM5 Catalysts for Nonoxidative Methane Conversion. *J. Phys. Chem. B* **1999**, *103* (28), 5787–5796. https://doi.org/10.1021/jp990866v.
(12) Tessonnier, J.-P.; Louis, B.; Walspurger, S.; Sommer, J.; Ledoux, M.-J.; Pham-Huu, C. Quantitative Measurement of the Brönsted Acid Sites in Solid Acids: Toward a Single-Site Design of Mo-Modified ZSM-5 Zeolite. *J. Phys. Chem. B* **2006**, *110* (21), 10390–10395. https://doi.org/10.1021/jp0602629.
(13) Tessonnier, J.-P.; Louis, B.; Rigolet, S.; Ledoux, M. J.; Pham-Huu, C. Methane Dehydro-Aromatization on Mo/ZSM-5: About the Hidden Role of Brønsted Acid Sites. *Applied Catalysis A: General* **2008**, *336* (1), 79–88. https://doi.org/10.1016/j.apcata.2007.08.026.
(14) Kosinov, N.; Hensen, E. J. M. Reactivity, Selectivity, and Stability of Zeolite-Based Catalysts for Methane Dehydroaromatization. *Advanced Materials* **2020**, *32* (44), 2002565. https://doi.org/10.1002/adma.202002565.
(15) Kim, Y.-H.; Borry, R. W.; Iglesia, E. Genesis of Methane Activation Sites in Mo-Exchanged H–ZSM-5 Catalysts. *Microporous and Mesoporous Materials* **2000**, *35–36*, 495–509. https://doi.org/10.1016/S1387-1811(99)00245-0.
(16) Ding, W.; Li, S.; D Meitzner, G.; Iglesia, E. Methane Conversion to Aromatics on Mo/H-ZSM5: Structure of Molybdenum Species in Working Catalysts. *J. Phys. Chem. B* **2001**, *105* (2), 506–513. https://doi.org/10.1021/jp0030692.
(17) Khatib, S. J.; Rahman, M.; Sridhar, A. Impact of the Presence of Mo Carbide Species Prepared Ex Situ in Mo/HZSM-5 on the Catalytic Properties in Methane Aromatization. *Applied Catalysis A: General* **2018**, *558*, 67–80.
(18) Vollmer, I.; Yarulina, I.; Kapteijn, F.; Gascon, J. Progress in Developing a Structure-Activity Relationship for the Direct Aromatization of Methane. *ChemCatChem* **2019**, *11* (1), 39–52. https://doi.org/10.1002/cctc.201800880.
(19) Çağlayan, M.; Paioni, A. L.; Dereli, B.; Shterk, G.; Hita, I.; Abou-Hamad, E.; Pustovarenko, A.; Emwas, A.-H.; Dikhtiarenko, A.; Castaño, P.; et al. Illuminating the Intrinsic Effect of Water Co-Feeding on Methane Dehydroaromatization: A Comprehensive Study. *ACS Catal.* **2021**, 11671–11684. https://doi.org/10.1021/acscatal.1c02763.
(20) Boltz, M.; Losch, P.; Louis, B. A General Overview on the Methanol to Olefins Reaction: Recent Catalyst Developments. **2013**. https://doi.org/info:doi/10.1166/acl.2013.1032.
(21) Kosinov, N.; Uslamin, E. A.; Coumans, F. J. A. G.; Wijpkema, A. S. G.; Rohling, R. Y.; Hensen, E. J. M. Structure and Evolution of Confined Carbon Species during Methane Dehydroaromatization over Mo/ZSM-5. *ACS Catal.* **2018**, *8* (9), 8459–8467. https://doi.org/10.1021/acscatal.8b02491.
(22) Gao, W.; Qi, G.; Wang, Q.; Wang, W.; Li, S.; Hung, I.; Gan, Z.; Xu, J.; Deng, F. Dual Active Sites on Molybdenum/ZSM-5 Catalyst for Methane Dehydroaromatization: Insights from Solid-State NMR Spectroscopy. *Angewandte Chemie International Edition n/a* (n/a). https://doi.org/10.1002/anie.202017074.
(23) Ma, D.; Wang, D.; Su, L.; Shu, Y.; Xu, Y.; Bao, X. Carbonaceous Deposition on Mo/HMCM-22 Catalysts for Methane Aromatization: A TP Technique Investigation. *Journal of Catalysis* **2002**, *208* (2), 260–269. https://doi.org/10.1006/jcat.2002.3540.
(24) Jiang, H.; Wang, L.; Cui, W.; Xu, Y. Study on the Induction Period of Methane Aromatization over Mo/HZSM-5: Partial Reduction of Mo Species and Formation of Carbonaceous Deposit. *Catalysis Letters* **1999**, *57* (3), 95–102. https://doi.org/10.1023/A:1019087313679.

(25) Zhao, K.; Jia, L.; Wang, J. The Influence of the Si/Al Ratio of Mo/HZSM-5 on Methane Non-Oxidative Dehydroaromatization. *New journal of Chemistry* **2019**, *43*, 4130–4136.
(26) Song, Y.; Xu, Y.; Suzuki, Y.; Nakagome, H.; Ma, X.; Zhang, Z.-G. The Distribution of Coke Formed over a Multilayer Mo/HZSM-5 Fixed Bed in H2 Co-Fed Methane Aromatization at 1073K: Exploration of the Coking Pathway. *Journal of Catalysis* **2015**, *330*, 261–272. https://doi.org/10.1016/j.jcat.2015.07.017.
(27) Gu, Y.; Chen, P.; Yan, H.; Wang, X.; Lyu, Y.; Tian, Y.; Liu, W.; Yan, Z.; Liu, X. Coking Mechanism of Mo/ZSM-5 Catalyst in Methane Dehydroaromatization. *Applied Catalysis A: General* **2021**, 118019. https://doi.org/10.1016/j.apcata.2021.118019.
(28) Tempelman, C.; Hensen, E. J. M. On the Deactivation of Mo/HZSM-5 in the Methane Dehydroaromatization Reaction. *Applied Catalysis B: Environmental* **2015**, *176–177*, 731–739. https://doi.org/10.1016/j.apcatb.2015.04.052.
(29) Wang, N.; Dong, X.; Liu, L.; Cai, D.; Cheng, Q.; Wang, J.; Hou, Y.; Emwas, A.-H.; Gascon, J.; Han, Y. Probing the Catalytic Active Sites of Mo/HZSM-5 and Their Deactivation during Methane Dehydroaromatization. *Cell Reports Physical Science* **2021**, *2* (1), 100309. https://doi.org/10.1016/j.xcrp.2020.100309.
(30) Beale, A. M.; Agote-Aran, M.; Lezcano-Gonzalez, I. Determination of Molybdenum Species Evolution during Non-Oxidative Dehydroaromatization of Methane and Its Implications for Catalytic Performance. *ChemCatChem* **2019**, *11* (1), 473–480.
(31) Kresse, G.; Furthmüller, J. Efficiency of Ab-Initio Total Energy Calculations for Metals and Semiconductors Using a Plane-Wave Basis Set. *Computational Materials Science* **1996**, *6* (1), 15–50. https://doi.org/10.1016/0927-0256(96)00008-0.
(32) Kresse, G.; Furthmüller, J. Efficient Iterative Schemes for Ab Initio Total-Energy Calculations Using a Plane-Wave Basis Set. *Phys. Rev. B* **1996**, *54* (16), 11169–11186. https://doi.org/10.1103/PhysRevB.54.11169.
(33) Batonneau-Gener, I.; Sachse, A. Determination of the Exact Microporous Volume and BET Surface Area in Hierarchical ZSM-5. *The Journal of Physical Chemistry C* **2019**. https://doi.org/10.1021/acs.jpcc.8b11524.
(34) Cho, H. S.; Miyasaka, K.; Kim, H.; Kubota, Y.; Takata, M.; Kitagawa, S.; Ryoo, R.; Terasaki, O. Study of Argon Gas Adsorption in Ordered Mesoporous MFI Zeolite Framework. *J. Phys. Chem. C* **2012**, *116* (48), 25300–25308. https://doi.org/10.1021/jp306268d.
(35) Abdolrahmani, M.; Chen, K.; White, J. L. Assessment, Control, and Impact of Brønsted Acid Site Heterogeneity in Zeolite HZSM-5. *J. Phys. Chem. C* **2018**, *122* (27), 15520–15528. https://doi.org/10.1021/acs.jpcc.8b04283.
(36) Jong, K. P. de. *Synthesis of Solid Catalysts*; John Wiley & Sons, 2009.
(37) Li, G.; Vollmer, I.; Liu, C.; Gascon, J.; Pidko, E. A. Structure and Reactivity of the Mo/ZSM-5 Dehydroaromatization Catalyst: An Operando Computational Study. *ACS Catal.* **2019**, *9* (9), 8731–8737. https://doi.org/10.1021/acscatal.9b02213.
(38) Rice, M. J.; Chakraborty, A. K.; Bell, A. T. Al Next Nearest Neighbor, Ring Occupation, and Proximity Statistics in ZSM-5. *Journal of Catalysis* **1999**, *186* (1), 222–227. https://doi.org/10.1006/jcat.1999.2544.
(39) Hu, H.; Wachs, I. E.; Bare, S. R. Surface Structures of Supported Molybdenum Oxide Catalysts: Characterization by Raman and Mo L3-Edge XANES. *J. Phys. Chem.* **1995**, *99* (27), 10897–10910. https://doi.org/10.1021/j100027a034.
(40) Gao, J.; Zheng, Y.; Jehng, J.-M.; Tang, Y.; Wachs, I. E.; Podkolzin, S. G. Identification of Molybdenum Oxide Nanostructures on Zeolites for Natural Gas Conversion. *Science* **2015**, *348* (6235), 686–690. https://doi.org/10.1126/science.aaa7048.
(41) Pinglian, T.; et al. Ammonia-Basified 10 Wt% Mo/HZSM-5 Material with Enhanced Dispersion of Mo and Performance for Catalytic Aromatization of Methane. *Applied Catalysis A: General* **2019**, *580*, 111–120.

(42) Wang, D.; Lunsford, J. H.; Rosynek, M. P. Characterization of a Mo/ZSM-5 Catalyst for the Conversion of Methane to Benzene. *Journal of Catalysis* **1997**, *169* (1), 347–358. https://doi.org/10.1006/jcat.1997.1712.
(43) Ma, D.; Shu, Y.; Cheng, M.; Xu, Y.; Bao, X. On the Induction Period of Methane Aromatization over Mo-Based Catalysts. *Journal of Catalysis* **2000**, *194* (1), 105–114. https://doi.org/10.1006/jcat.2000.2908.
(44) Ma, D.; Shu, Y.; Zhang, W.; Han, X.; Xu, Y.; Bao, X. In Situ 1H MAS NMR Spectroscopic Observation of Proton Species on a Mo-Modified HZSM-5 Zeolite Catalyst for the Dehydroaromatization of Methane. *Angewandte Chemie International Edition* **2000**, *39* (16), 2928–2931. https://doi.org/10.1002/1521-3773(20000818)39:16<2928::AID-ANIE2928>3.0.CO;2-T.
(45) Cui, Y.; Xu, Y.; Suzuki, Y.; Zhang, Z.-G. Experimental Evidence for Three Rate-Controlling Regions of the Non-Oxidative Methane Dehydroaromatization over Mo/HZSM-5 Catalyst at 1073 K. *Catal. Sci. Technol.* **2011**, *1* (5), 823–829. https://doi.org/10.1039/C1CY00083G.
(46) Razdan, N. K.; Bhan, A. Carbidic Mo Is the Sole Kinetically-Relevant Active Site for Catalytic Methane Dehydroaromatization on Mo/H-ZSM-5. *Journal of Catalysis* **2020**, *389*, 667–676. https://doi.org/10.1016/j.jcat.2020.06.035.
(47) Sun, X.; Mueller, S.; Shi, H.; Haller, G. L.; Sanchez-Sanchez, M.; van Veen, A. C.; Lercher, J. A. On the Impact of Co-Feeding Aromatics and Olefins for the Methanol-to-Olefins Reaction on HZSM-5. *Journal of Catalysis* **2014**, *314*, 21–31. https://doi.org/10.1016/j.jcat.2014.03.013.
(48) Chen, N. Y.; Reagan, W. J. Evidence of Autocatalysis in Methanol to Hydrocarbon Reactions over Zeolite Catalysts. *Journal of Catalysis* **1979**, *59* (1), 123–129. https://doi.org/10.1016/S0021-9517(79)80050-0.
(49) Xu, S.; Zhi, Y.; Han, J.; Zhang, W.; Wu, X.; Sun, T.; Wei, Y.; Liu, Z. Chapter Two - Advances in Catalysis for Methanol-to-Olefins Conversion. In *Advances in Catalysis*; Song, C., Ed.; Academic Press, 2017; Vol. 61, pp 37–122. https://doi.org/10.1016/bs.acat.2017.10.002.
(50) Beuque, A.; Barreau, M.; Berrier, E.; Paul, J.-F.; Batalha, N.; Sachse, A.; Pinard, L. Transformation of Dilute Ethylene at High Temperature on Micro- and Nano-Sized H-ZSM-5 Zeolites. *Catalysts* **2021**, *11* (2), 282. https://doi.org/10.3390/catal11020282.
(51) Vollmer, I.; Abou-Hamad, E.; Gascon, J.; Kapteijn, F. Aromatization of Ethylene – Main Intermediate for MDA? *ChemCatChem* **2020**, *12* (2), 544–549. https://doi.org/10.1002/cctc.201901655.
(52) Levenspiel, O. Experimental Search for a Simple Rate Equation to Describe Deactivating Porous Catalyst Particles. *Journal of Catalysis* **1972**, *25* (2), 265–272. https://doi.org/10.1016/0021-9517(72)90227-8.
(53) Bartholomew, C. H. Mechanisms of Catalyst Deactivation. *Applied Catalysis A: General* **2001**, *212* (1), 17–60. https://doi.org/10.1016/S0926-860X(00)00843-7.
(54) Ma, H.; Kojima, R.; Kikuchi, S.; Ichikawa, M. Effective Coke Removal in Methane to Benzene (MTB) Reactionon Mo/HZSM-5 Catalyst by H2 and H2O Co-Addition to Methane. *Catal Lett* **2005**, *104* (1), 63–66. https://doi.org/10.1007/s10562-005-7437-y.
(55) Natesakhawat, S.; Means, N. C.; Howard, B. H.; Smith, M.; Abdelsayed, V.; Baltrus, J. P.; Cheng, Y.; Lekse, J. W.; Link, D.; Morreale, B. D. Improved Benzene Production from Methane Dehydroaromatization over Mo/HZSM-5 Catalysts via Hydrogen-Permselective Palladium Membrane Reactors. *Catal. Sci. Technol.* **2015**, *5* (11), 5023–5036. https://doi.org/10.1039/C5CY00934K.
(56) Kinage, Anil. K.; Ohnishi, R.; Ichikawa, M. Marked Enhancement of the Methane Dehydrocondensation Toward Benzene Using Effective Pd Catalytic Membrane Reactor with Mo/ZSM-5. *Catalysis Letters* **2003**, *88* (3), 199–202. https://doi.org/10.1023/A:1024022124804.
(57) Larachi, F.; Oudghiri-Hassani, H.; Iliuta, M. C.; Grandjean, B. P. A.; McBreen, P. H. Ru-Mo/HZSM-5 Catalyzed Methane Aromatization in Membrane Reactors. *Catalysis Letters* **2002**, *84* (3), 183–192. https://doi.org/10.1023/A:1021475819517.

(58) Ben Tayeb, K.; Hamieh, S.; Canaff, C.; Nguyen, H.; Vezin, H.; Pinard, L. The Radical Internal Coke Structure as a Fingerprint of the Zeolite Framework. *Microporous and Mesoporous Materials* **2019**, *289*, 109617. https://doi.org/10.1016/j.micromeso.2019.109617.
(59) Guisnet, M.; Magnoux, P. Organic Chemistry of Coke Formation. *Applied Catalysis A: General* **2001**, *212* (1), 83–96. https://doi.org/10.1016/S0926-860X(00)00845-0.
(60) A. Pimenta, M.; Dresselhaus, G.; S. Dresselhaus, M.; G. Cançado, L.; Jorio, A.; Saito, R. Studying Disorder in Graphite -Based Systems by Raman Spectroscopy. *Physical Chemistry Chemical Physics* **2007**, *9* (11), 1276–1290. https://doi.org/10.1039/B613962K.
(61) Guisnet, M.; Costa, L.; Ribeiro, F. R. Prevention of Zeolite Deactivation by Coking. *Journal of Molecular Catalysis A: Chemical* **2009**, *305* (1), 69–83. https://doi.org/10.1016/j.molcata.2008.11.012.

Table and figures

Table 1: Textural and acidic properties of the H-ZSM-5 before and after Mo impregnation.

Figure 1: Characterization of the H-ZSM-5 before (in black) and after Mo impregnation (in red): (a) N_2 adsorption and desorption nitrogen isotherms at -196 °C, (b) IR spectra of OH region, (c) Raman spectra, and XRD patterns.

Figure 2: (a) Ion abundance of benzene as a function of a long time-on-stream, (b) for different contact times during activation and inductions, and (c) duration of these two steps as a function of contact time.

Figure 3: Amount of reacted methane during the activation period as a function of the molybdenum oxide in the catalytic bed.

Figure 4: Reaction mechanism for diffusion into zeolite and activation of the first CH_4 for the catalytic MDA reaction on $[Mo_2C_2]^{2+}$ system at 700 °C.

Figure 5: (a) Initial molar conversion of methane, (b) formation rate of hydrogen, mass yields of (c) ethylene, (d) benzene, (e) toluene, and (f) naphthalene as a function of contact time. The yellow square is a magnified area at the lower contact times.

Figure 6: (a) Molar conversion of methane, (b) hydrogen formation rate, and corresponding (c) deactivation constant as a function of time on steam for different contact times.

Figure 7: (a) Formation rate of hydrogen, mass yields of (b) ethylene, (c) benzene, (d) toluene, (e) naphthalene as a function of the methane conversion for different contact time.

Figure 8: (a) Example of thermogravimetric analysis of a spent catalyst (τ = 0.85 s) with associated (b) CO_2 and (c) H_2O profiles, deconvoluted into two peaks: in blue, “soft” coke, and in red, “hard” coke.

Figure 9: (a) Total, "soft", and "hard" coke contents and (b) weight gain as a function of contact time. (c) "Soft" and (d) "hard" coke contents vs. deactivation constant (k_d).

Figure 10: Evolution vs. contact time of the nature of the “soft” and “hard” coke characterized by the molar ratios of C/H^+ and C/Mo, respectively.

Figure 11: (a) Analysis of both 1350 (black) and 1595 cm^{-1} (red) Raman peaks -typical of polyaromatic hydrocarbons- recorded along the TPO of the spent catalyst Sp/2.04: evolution of peak area as a function of temperature (plain lines) and corresponding derivative (dot-dashed lines). (b) CO_2 production measured online -simultaneously to the collection of Raman spectra shown in (a) and decomposition into Gauss curves.

Figure 12: Computed structures of (a) benzene, (b) naphthalene, (c) benzene co-adsorption H_2 and (d) naphthalene co-adsorbed H_2 adsorbed at Mo_2C_2 active site located at δ-channels of ZSM-5 and corresponding adsorption energies.

New insights towards four successive stages in methane dehydroaromatization reaction over Mo/H-ZSM-5 catalyst.

Antoine Beuque 1, Hu Hao, Elise Berrier 2, Nuno Batalha 1, Alexander Sachse 1, Jean-François Paul* [2,] Ludovic Pinard [1,*]**

[1]Institut de Chimie des Milieux et Matériaux de Poitiers (ICM2P), UMR 7285 CNRS, 4 Rue Michel Brunet, Bâtiment B27, 86073 Poitiers Cedex 9–France;

[2]Univ. Lille, CNRS, Centrale Lille, Univ. Artois, UMR 8181–UCCS–Unité de Catalyse et Chimie du Solide, F-59000 Lille, France.

Supporting Information

Table S1: Comparison of the spent catalysts recovered after 10 hours of reaction.

Figure S1: Position of monomeric $[MoO_2]^{2+}$ and dimeric $[Mo_2O_5]^{2+}$species in the zeolite channel (Mo-blue, Al pink, Si yellow).

Figure S2: Ion abundance of (a) methane, (b) ethylene, (c) toluene, and (d) naphthalene as a function of the time on stream for different contact times.

Figure S3: TGA profile of commercial Mo_2C.

Figure S4: Residual microporous volume and residual Brønsted acidity as a function of total coke content

Figure S5 Coke amount calculated from the TG analysis as a function of the carbon content calculated from elemental analysis.

Figure S6: H/C molar ratio of the spent samples recovered as function of the contact time, (b) H/C molar ratio and the density of reference coke molecules generally trapped within the zeolite HZSM-5

Figure S7: Cumulative amount of hydrogen produced after 10 hours of reaction as a function of the total coke content.

Figure S8: Evolution of Raman signature of spent catalyst collected during its TPO. Note that the fluorescence contribution has been removed by a baseline subtraction.

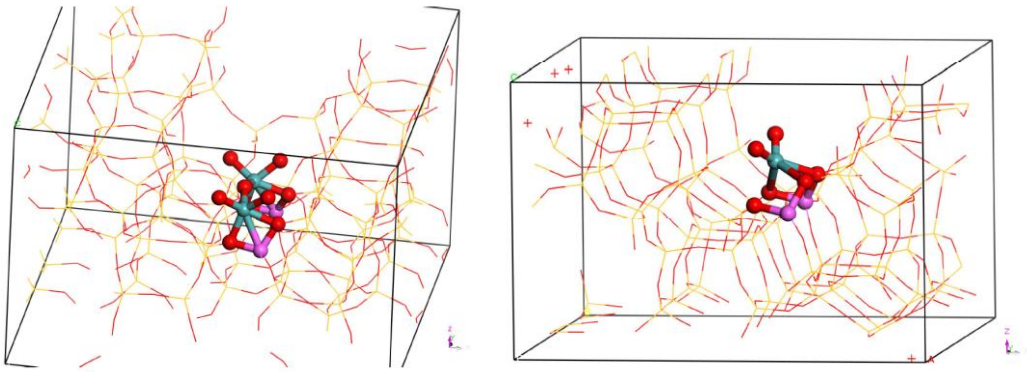

Figure S1: Position of monomeric $[MoO_2]^{2+}$ and dimeric $[Mo_2O_5]^{2+}$species in the zeolite channel (Mo-blue, Al pink, Si yellow)

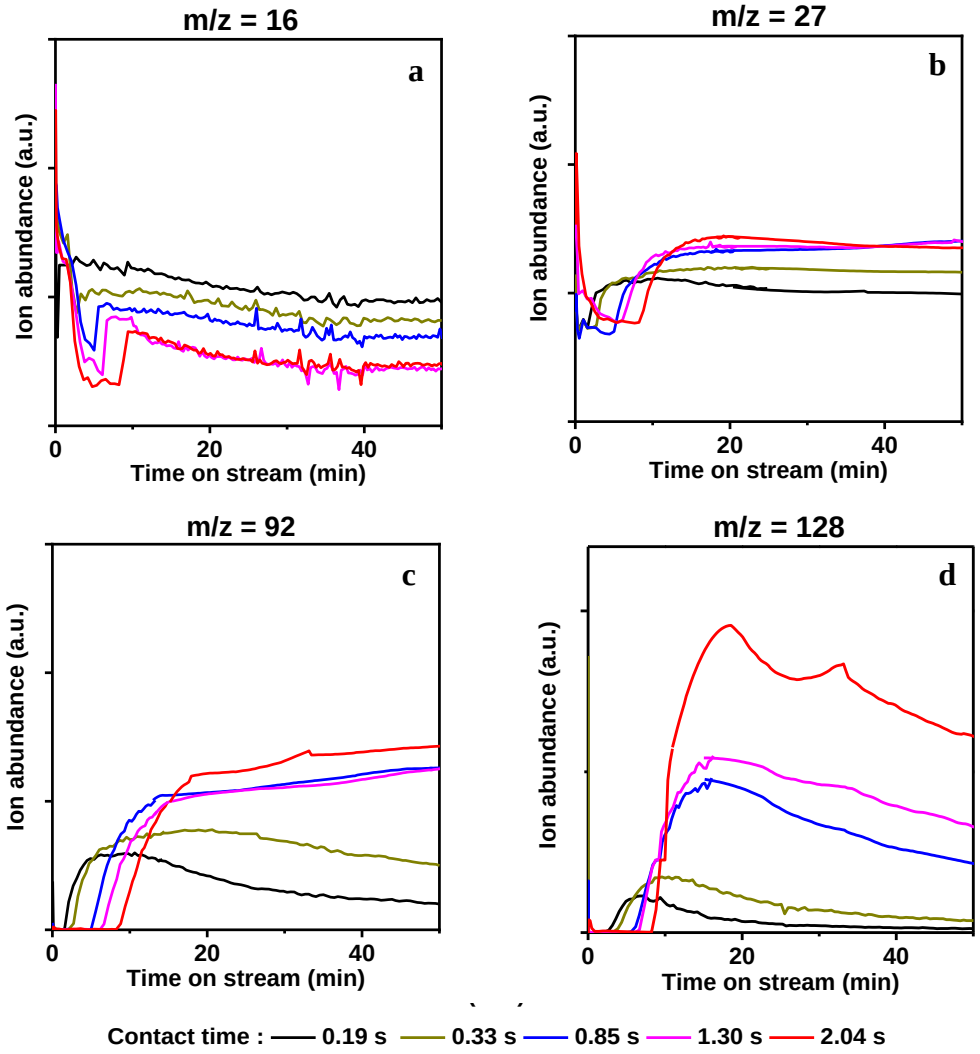

Figure S2: Ion abundance of (a) methane, (b) ethylene, (c) toluene and (d) naphthalene as a function of the time on stream for different contact times.

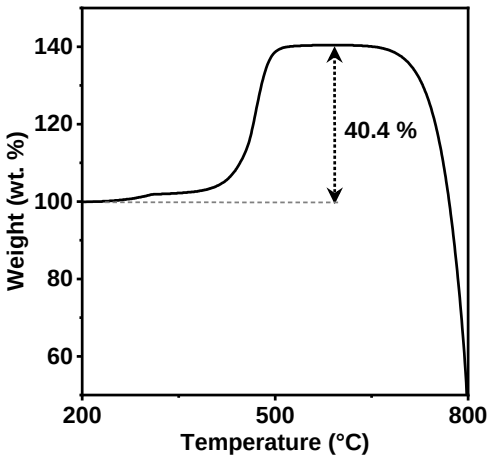

Figure S3: TGA profile of commercial Mo_2C.

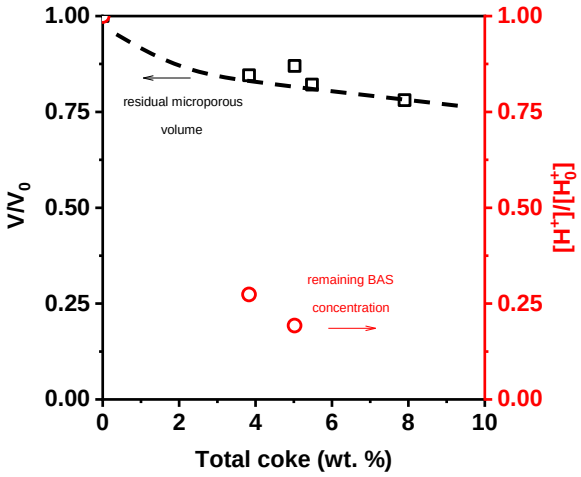

Figure S4: Residual microporous volume and residual Brønsted acidity as a function of total coke content.

Remark: Only two pyridine adsorption monitored by FT-IR spectroscopy on the spent catalyst containing the less carbon could be carried out. At higher coke content the intensity saturated.

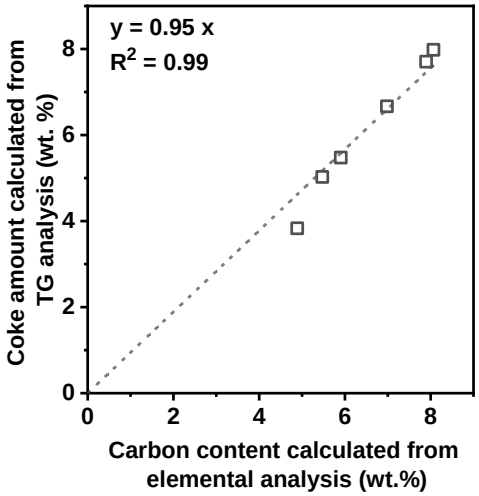

Figure S5: Coke amount calculated from the TG analysis as a function of the carbon content calculated from elemental analysis.

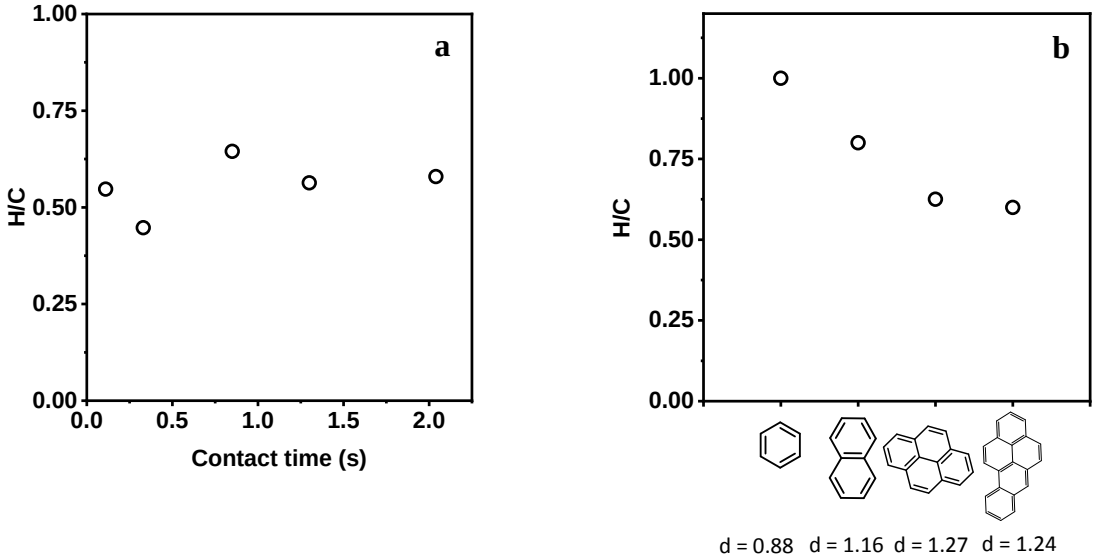

Figure S6: (a) H/C molar ratio of the spent samples recovered as function of the contact time, (b) H/C molar ratio and the density of reference coke molecules generally trapped within the zeolite HZSM-5

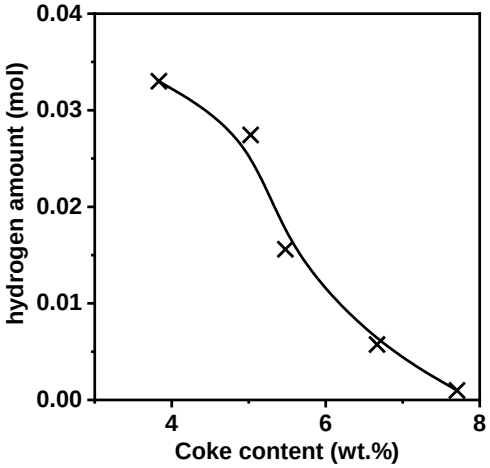

Figure S7: Cumulative amount of hydrogen produced after 10 hours of reaction as a function of the total coke content.

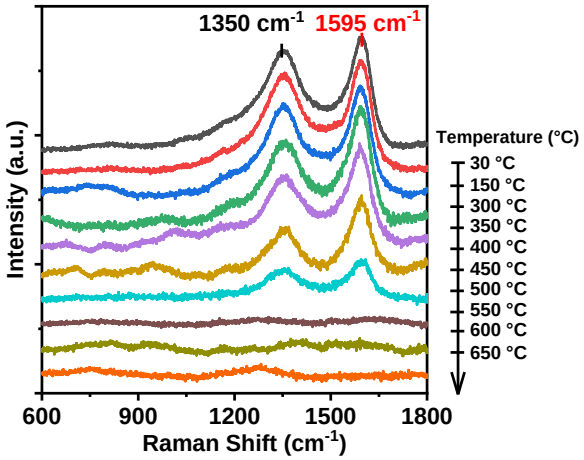

Figure S8: Evolution of Raman signature of spent catalyst collected during its TPO. Note that the fluorescence contribution has been removed by a baseline subtraction.

Sample	Carbidic coke [a]	"Soft" coke[a]		"Hard" coke[a]		H/C[b]	BrØnsted acidity[c]		Micropore volume[d]		deactivation rate (h. g_{cat}^{-1})[e]	
	(wt.%)	(wt.%)	mg/g_{cat}	Amount (wt.%)	mg/g_{cat}		Value (µmol. g_{cat}^{-1})	Reduction (%)	Value (cm^3 g_{cat}^{-1})	Reduction (%)	Methane	Hydrogen
Sp/0.11	0.15	4.6	48.0	3.6	37.3	0.55			0.09	25	0.51	0.70
Sp/0.33	0.16	3.6	37.9	3.0	31.1	0.44					0.47	0.64
Sp/0.85	0.13	3.3	34.2	2.2	22.2	0.64			0.10	16	0.33	0.42
Sp/1.30	0.09	3.5	36.7	1.5	15.0	0.56	62	72	0.10	17	0.26	0.35
Sp/2.04	0.06	3.4	34.9	0.5	4.6	0.58	88	60	0.10	13	0.15	0.37

Table S.1: Comparison of the spent catalysts recovered after 10 hours of reaction

[a] measured by thermogravimetry analysis, [b] the molar ratio H/C was calculated from elementary analysis and represent the ratio of the total coke [c] the Brønsted acid sites probed by themodesorption of pyridine at 150 °C, [d] the micropore volume (V_{micro}) was calculated from the t-plot curve using the Harkins-Jura method and a thickness range between 4.5 and 5.5 Å, [e] the deactivation rate is the slope of the logarithmic plot of the methane conversion rate and hydrogen formation rate